



## OPEN Operation mechanism analysis and parameter optimization of airflow-rotating disc separation device for agricultural film fragments

Jiali Li<sup>1,3</sup>, Huijie Peng<sup>1,3</sup>, Xinzhong Wang<sup>2</sup>, Fengling Dou<sup>1</sup>, Yefan Chen<sup>1,3</sup>, Hwei Meng<sup>1,3</sup>✉ & Za Kan<sup>1,3</sup>✉

To reduce the impurity and loss rates during agricultural film fragment separation, an integrated airflow and mechanical separation approach was devised, and the airflow-rotating disc separation device with air suction mechanism and curved disc rotating screening mechanism was designed. The processes of throwing, collision and slipping were analyzed, considering film compressibility. The factors affecting the separation performance were identified as feeding quantity, airflow velocity and disc rotational velocity. Subsequently, a Box-Behnken response surface experiment was conducted, using fan rotational velocity, disc rotational velocity, and feeding quantity as factors, with impurity removal rate and film leakage rate as the evaluation indices. The multiple regression equations were established to depict the relationships between the factors and the indices, followed by the response surface analysis. The optimal parameter combination was a fan rotational velocity of 1450 r/min, a disc rotational velocity of 54 r/min, and a feeding quantity of 130 kg/h, attaining an impurity removal rate of 96.51% and a film leakage rate of 21.92%. The discrepancies between the verification values and the prediction values were 4.61% and 5.30% respectively, signifying the equations' reliable predictability. This research lays the groundwork for the design of film fragment separation apparatuses.

**Keywords** Agricultural machinery, Plastic film, Kinetic analysis, Screening mechanism

Plastic film mulching technology has been widely adopted in cotton plantations in Xinjiang, leading to a significant increase in cotton yields<sup>1</sup>. However, repeated use of this mulching technique over successive years has resulted in the gradual accumulation of residual films in the fields, posing a serious threat to both the ecological environment and agricultural productivity<sup>2</sup>. While the development and implementation of residual film recycling machinery have alleviated the pollution caused by film residues to some extent<sup>3,4</sup>, the recovered films are often mixed with cotton straw and soil, which severely hinder their subsequent recycling and utilization<sup>5</sup>. At present, although agricultural residual films are recycled, they are not effectively reused. Instead, they are typically piled up, discarded, or buried in situ, leading to resource wastage and secondary environmental pollution<sup>6,7</sup>. Therefore, there is an urgent need for research into technologies for separating films from impurities.

Currently, the most used technology for separating residual films from impurities is airflow-screen separation. This method enhances the dispersion of the mixture on the sieve surface through the combined effects of airflow and vibration, improving the stratification and sieve-through efficiency of different components<sup>8</sup>, thereby enabling the separation of residual films and impurities. The most widely used equipment for this process is the airflow-drum screen, with impurity content in the separated films ranging from 5.86 to 13.71%. It is driven by the idler roller transmission method, making the rotating drum rotate around the axis. The cross-sectional area of the screen drum shaft is about 2.24 m<sup>2</sup>, and the working efficiency is 202 kg/h ~ 250 kg/h. Thus, the working efficiency per unit area can be calculated as 90 kg/h ~ 112 kg/h<sup>9-11</sup>. The airflow-vibrating screen is also applied, with impurity content in the separated films about 3.08%. It adopts a belt-drive system to actuate the double-crank connecting-rod mechanism, causing the sieve surface to vibrate. The working area is approximately 2.10 m<sup>2</sup>, and the working efficiency is 1026 kg/h. Thus, the working efficiency per unit area can be calculated as 489 kg/h<sup>12</sup>. However, one major limitation is that the screen holes can easily become blocked

<sup>1</sup>College of Mechanical and Electrical Engineering, Shihezi University, Shihezi, Xinjiang 832000, China. <sup>2</sup>School of Agricultural Engineering, Jiangsu University, Zhenjiang 212013, China. <sup>3</sup>Engineering Research Centre of Ministry of Education for Mechanization of Production of Oasis Characteristic Cash Crops, Shihezi 832000, China. ✉email: mh\_w\_mac@shzu.edu.cn; kz\_mac@shzu.edu.cn

by the films during separation, leading to a decline in operational performance<sup>13,14</sup>. This blockage issue is also observed in other screening equipment, such as the jitter screen used in corn harvesters<sup>15</sup>, the vibrating screen in rapeseed combine harvesters<sup>16</sup>, and the drum screens in urban solid waste processing<sup>17</sup>. To address this problem, researchers have enhanced the cleaning mechanism of sieves by integrating machine vision and bionic technology, which improves performance but also increases the complexity and energy consumption of the equipment. In contrast, the airflow-rotating disc film impurity separation device proposed in this study uses a chain drive system to rotate the main shaft and the driven shaft, thereby making the discs turn. The working area is approximately 0.78 m<sup>2</sup>, and the working efficiency is 130 kg/h. Thus, the working efficiency per unit area can be calculated as 167 kg/h. Moreover, the dynamic sieve holes with forced displacement drive the materials to continuously move towards the sieve tail, actively clean the sieve holes, and reduce the possibility of material blockage<sup>18</sup>. Compared with vibrating and drum screens, the device features a simple transmission method and component structure, a high energy-consumption utilization rate, a strong self-cleaning ability for sieve holes, and relatively low difficulty in equipment manufacturing and maintenance.

The complex dynamic behavior of residual films and impurities interferes with the transport process and affects separation efficiency. Understanding the motion characteristics of these materials is crucial for analyzing the causes of incomplete separation. Zhang (2024) and Peng (2021) analyzed the critical conditions for the sliding, downward motion, and ejection of soil and residual film along the sieve surface under crank linkage action<sup>12,19</sup>. Zhou et al. (2023) examined the critical rotational speed conditions for sliding, throwing, and centrifugal motion in a drum screen<sup>20</sup>. Most research on the motion characteristics of films and impurities has focused on critical condition analysis based on D'Alembert's principle and Newton's second law, and has paid less attention to the motion behaviors before and after the critical state or the interactions between different motion phases. In contrast, Song et al. (2023), Fang et al. (2020; 2021), and Wang et al. (2019) classified the multi-process motions of materials such as *Fritillaria ussuriensis* Maxim (FUM), straw, and grain into distinct chronological stages. These stages were interconnected through velocity continuity<sup>21–24</sup>, offering a more comprehensive analysis of the complex dynamic behavior of materials. This approach provides valuable insights for studying the motion characteristics of residual films and impurities.

Based on the studies mentioned above, a novel separation method for films and impurities has been investigated, which utilizes the dual-action of airflow and rotational disc mechanical separation. By integrating the effects of airflow and disc motion, this approach combines two forces innovatively to enhance material separation. A systematic study of the separation process has been conducted, with a focus on the key stages of material throwing, collision with the disc, and relative slipping of components. Additionally, a relationship model has been established, linking fan velocity, disc rotational velocity, and feeding quantity with both the impurity removal rate and the film leakage rate. This model provides valuable insights for optimizing the separation process. Overall, the research offers a solid theoretical foundation for the development of advanced separation technologies for films and impurities.

## Theory and analysis of film and impurity materials separation process Structure and working principle of the separation device

Figure 1 vividly presents the three-dimensional structural schematic diagram of the airflow-rotating disc film impurity separation device, which was drawn by SolidWorks 2022 software. As shown in Fig. 1, the separation device is mainly composed of a feeding conveyor, elevator, disc sieve, suction hood, pipeline, cotton impurity collection box, residual film collection box, fan, receiving conveyor and soil impurity collection box. Crucially, the main structural parameters, which play a fundamental role in the device's performance, related to the disc sieve are detailed in Table 1. To further elaborate on the components, the disc sieve and suction hood, which are important working parts of the device, achieve the separation of residual film and impurities through their synergistic effect with the disc and airflow. Their specific details are presented in the following figures: Fig. 2 shows the arrangement of sieve discs, and Fig. 3 displays the structure of the suction hood.

The working principle of this device is as follows: when the device works normally, the film and impurity materials are transported to the elevator through the feeding conveyor, and then transported to the disc sieve. Under the action of transportation and loosening of the sieve, the smaller-sized soil and straw impurities fall into the receiving conveyor through the gaps between the discs, and are transported to the soil impurity collection box. Simultaneously, the remaining materials are transported to the end of the disc sieve. When the materials pass below the suction hood, the films enter the residual film collection box under the action of airflow, and the large stones and straw impurities continue to be transported to the cotton impurity collection box.

### Analysis of separation process

Figure 4 shows the motion trajectory of the film and impurity materials on the disc sieve. From  $P_1$  to  $P_4$ , the materials go through different motion stages with complex force conditions closely related to the airflow and disc sieve movement. The motion of the materials under the dual action comprises four stages: (1) Before the collision with the sieve disc: the throwing process in the windless area ( $P_1 \sim P_2$  stage); (2) Before the collision with the sieve disc: the throwing process in the windy area ( $P_2 \sim P_3$  stage); (3) Collision stage with the sieve disc ( $P_3$  stage); (4) After the collision: the relative slipping of cotton straw, soil and residual film to the separation stage ( $P_3 \sim P_4$  stage).

- (1) The throwing process in the windless area ( $P_1 \sim P_2$  stage).

Figure 5 shows the force analysis of the throwing process in the windless area ( $P_1 \sim P_2$  stage). The film and impurity materials are thrown from point  $P_1$  to point  $P_2$ , with an initial velocity of  $v_0$  and a horizontal angle of  $\alpha_0$ .

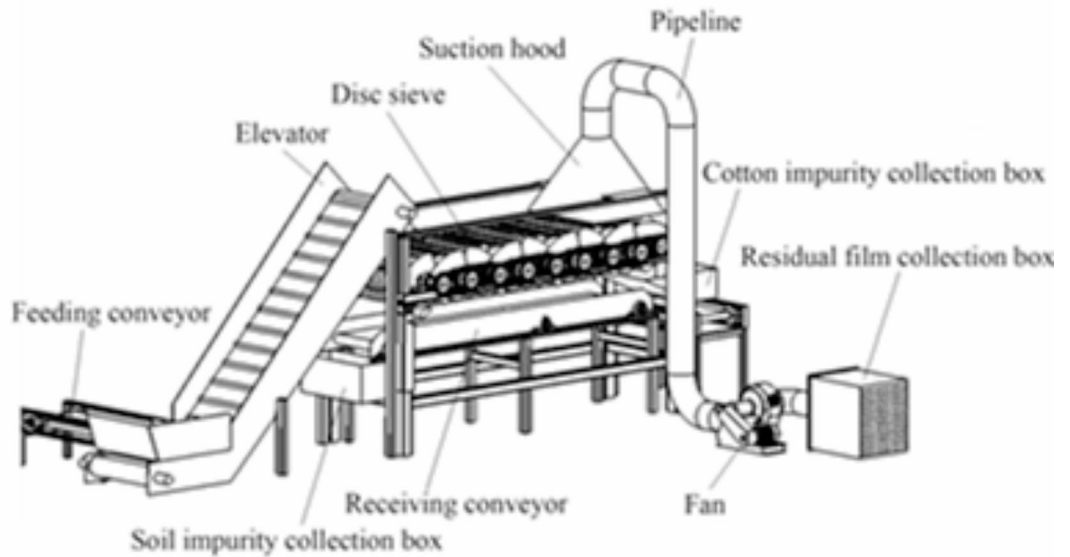


**Fig. 1.** Airflow-rotating disc film impurity separation device. The overall structure of the device, along with the relative positional relationship, connection, and layout of each component, is shown, with these components working in concert to achieve the separation of agricultural film and impurities.

Parameter	Value
Overall dimensions of length, width and height, $L \times W \times H$ , mm $\times$ mm $\times$ mm)	2200 $\times$ 1500 $\times$ 1300
Matching power (kW)	7
Disc sieve working width ( $W_w$ , mm)	520
Radius of the curved edge of the irregular sieve disc ( $R$ , mm)	270
Number of irregular sieve discs (pcs)	243

**Table 1.** Comprehensive overview of the main structural parameters of the disc sieve: dictating installation prerequisites.

At this stage, the materials are subjected to gravity  $G$ . Ignoring the air resistance, Eq. (1) represents the motion model of the materials in the  $0 \sim t_1$  time.

$$\begin{cases} m \frac{dv_{1x}}{dt} = 0 \\ m \frac{dv_{1y}}{dt} = -G = -mg \end{cases} \quad (1)$$

where,  $m$  is the mass of the film and impurity materials, kg;  $g$  is the acceleration of gravity,  $9.81 \text{ m/s}^2$ .

The initial conditions are as follows:  $t = 0, v_{0x} = v_0 \cos \alpha_0, v_{0y} = v_0 \sin \alpha_0, x_0 = 0$ , and  $y_0 = 0$ . Then, Eqs. (2) and (3) are obtained by taking the first-order and the second-order integrals of Eq. (1), respectively.

$$\begin{cases} v_{1x} = v_0 \cos \alpha_0 \\ v_{1y} = v_0 \sin \alpha_0 - gt_1 \end{cases} \quad (2)$$

$$\begin{cases} x_1 = v_0 t_1 \cos \alpha_0 \\ y_1 = v_0 t_1 \sin \alpha_0 - \frac{1}{2} g t_1^2 \end{cases} \quad (3)$$

where,  $x_1$  is the displacement of the material in the  $x$ -direction after the movement of  $t_1$  time, m;  $y_1$  is the displacement of the material in the  $y$ -direction after the movement of  $t_1$  time, m.

(2) The throwing process in the windy area ( $P_2 \sim P_3$  stage).

Figure 6 shows the force analysis of the throwing process in the windy area ( $P_2 \sim P_3$  stage). When the film and impurity materials move from point  $P_2$  to point  $P_3$ , they are subjected to the gravity  $G$  and wind force  $F_w$ .

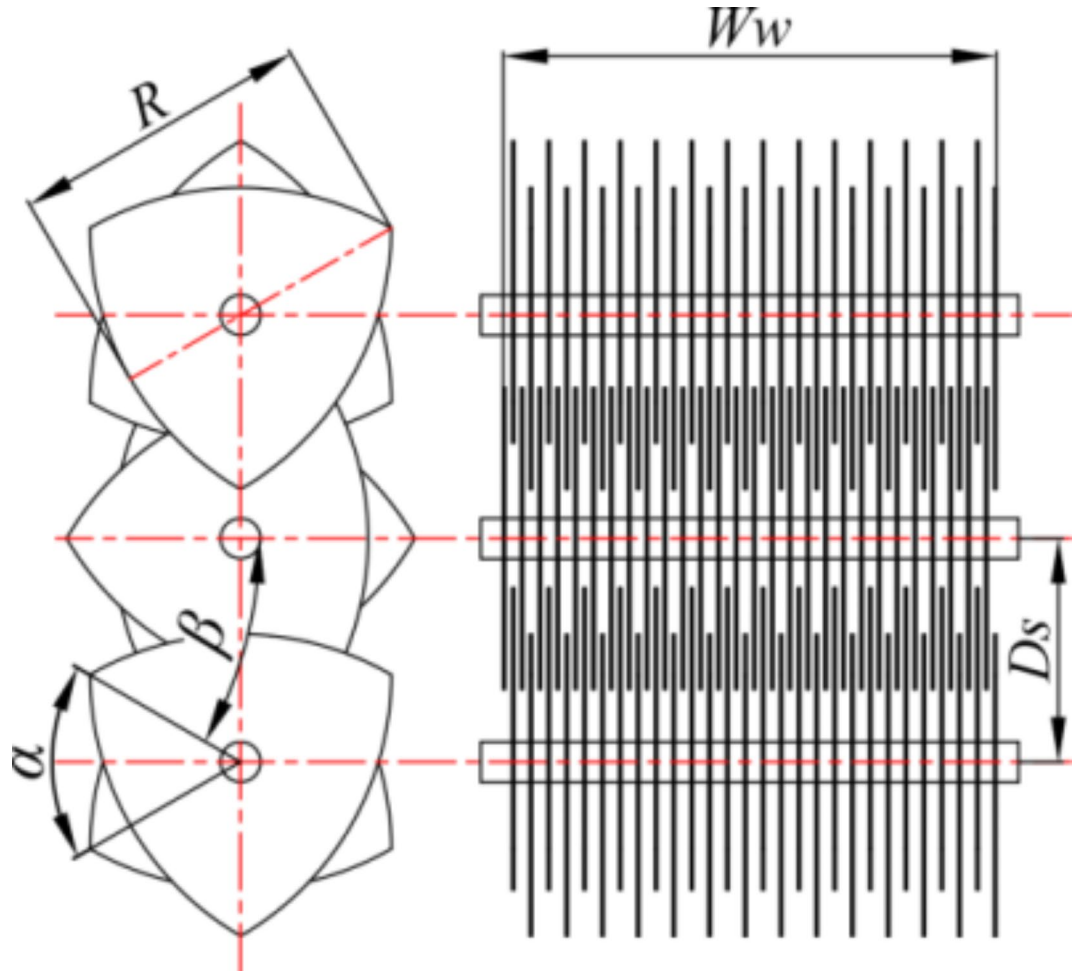


**Fig. 2.** Arrangement of sieve discs. The discs are arranged with adjacent ones on the same shaft having a 60° phase angle ( $\alpha$ ), those on adjacent shafts having a 30° angle ( $\beta$ ), in an interlaced pattern, and the adjacent shafts distance being 200 mm ( $D_s$ ).

At this stage, Eq. (4) represents the motion model of the material during the time interval from  $t_1$  to  $t_2$ .

$$\begin{cases} m \frac{dv_{2x}}{dt} = F_w \cos \beta \\ m \frac{dv_{2y}}{dt} = F_w \sin \beta - mg \\ F_w = \frac{1}{2} k \rho_0 S v^2 \\ S = L_1 L_2 \end{cases} \quad (4)$$

where,  $v_{2x}$  is the partial velocity of the material in the  $x$ -direction after the movement of  $t_2$  time, m/s;  $v_{2y}$  is the partial velocity of the material in the  $y$ -direction after the movement of  $t_2$  time, m/s;  $k$  is the airflow resistance coefficient;  $\rho_0$  is the density of the air, kg/m<sup>3</sup>;  $S$  is the film and impurity materials windward area, m<sup>2</sup>;  $L_1$  is the length of the materials, m;  $L_2$  is the width of the materials, m.

Combining Eqs. (2) and (3), (5) and (6) are obtained by taking the first-order and the second-order integrals of Eq. (4).

$$\begin{cases} v_{2x} = \frac{k \rho_0 S v^2}{2m} (t_2 - t_1) \cos \beta + v_0 \cos \alpha_0 \\ v_{2y} = \frac{k \rho_0 S v^2}{2m} (t_2 - t_1) \sin \beta + v_0 \sin \alpha_0 - g t_2 \\ v_2 = \sqrt{v_{2x}^2 + v_{2y}^2} \\ \alpha_1 = \arctan \left( \frac{v_{2y}}{v_{2x}} \right) \end{cases} \quad (5)$$

$$\begin{cases} x_2 = \frac{k \rho_0 S v^2}{4m} (t_2^2 - t_1^2) \cos \beta - \frac{k \rho_0 S v^2}{2m} t_1 (t_2 - t_1) \cos \beta + v_0 t_2 \cos \alpha_0 \\ y_2 = \frac{k \rho_0 S v^2}{4m} (t_2^2 - t_1^2) \sin \beta - \frac{k \rho_0 S v^2}{2m} t_1 (t_2 - t_1) \sin \beta + v_0 t_2 \sin \alpha_0 - \frac{1}{2} g t_2^2 \end{cases} \quad (6)$$

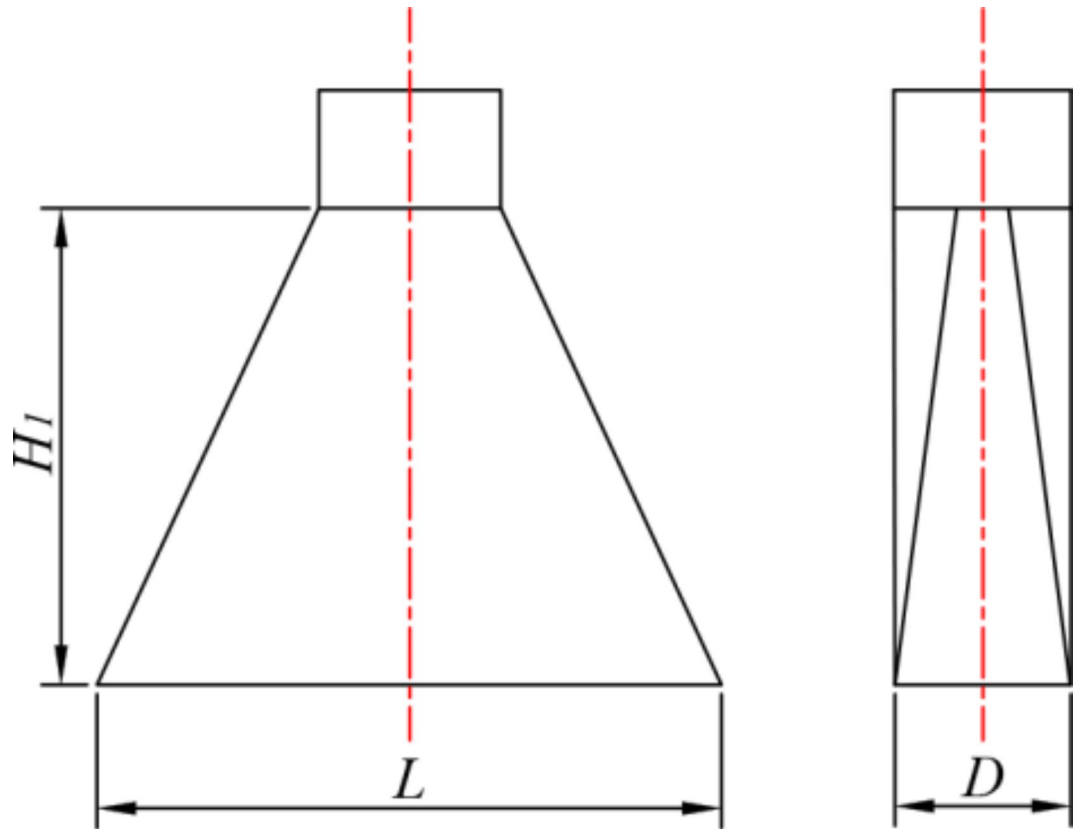


**Fig. 3.** Structure of suction hood. The suction hood has its main structural parameters with the length of the bottom ( $L$ ) being 520 mm, the height of the shoulder ( $H_1$ ) being 400 mm, and the bottom width ( $D$ ) being 150 mm.

where,  $\alpha_1$  is the angle between  $v_{2x}$  and  $v_2$ ;  $x_2$  is the displacement of the material in the  $x$ -direction after the movement of  $t_2$  time,  $m$ ;  $y_2$  is the displacement of the material in the  $y$ -direction after the movement of  $t_2$  time.

(3) Collision with the sieve disc ( $P_3$  stage).

In the study of the collision stage, the following assumptions are made: (1) inelastic collision occurs when the film and impurity materials collide with the sieve disc; (2) when a collision occurs, the changes in the displacement and velocity direction are neglected. Figure 7 shows the force analysis of the collision stage. The initial kinetic energy  $E_0$  of the material when it starts to contact the sieve disc and the final kinetic energy  $E_1$  after the collision are shown in Eq. (7).

$$\begin{cases} E_0 = \frac{1}{2}mv_2^2 \\ E_1 = \frac{1}{2}mv_3^2 \end{cases} \quad (7)$$

Due to the small relative velocity between the internal components of the film and impurity materials, the energy consumption during the collision is small. It is assumed that there is no energy loss in the system during the collision, and the initial kinetic energy  $E_0$  is transformed into the final kinetic energy  $E_1$  and deformation energy  $\Delta E$ . Then, the initial kinetic energy  $E_0$  can be expressed as Eq. (8).

$$\frac{1}{2}mv_2^2 = \frac{1}{2}mv_3^2 + \Delta E \quad (8)$$

During the collision, the sieve disc is mainly subjected to the impact force in the normal direction of the contact point. Combining Eq. (4), Eq. (9) represents the impact force  $F_{sm}$  of the materials.

$$F_{sm} = mg \cos \sigma - \frac{k\rho_0 S v^2}{2} \sin(\beta - \sigma) \quad (9)$$

Assume that the deformation of the film and impurity materials only occurs in the normal direction of the contact point with the sieve disc, with the maximum deformation amount being  $\delta$ . Combined with Newton's

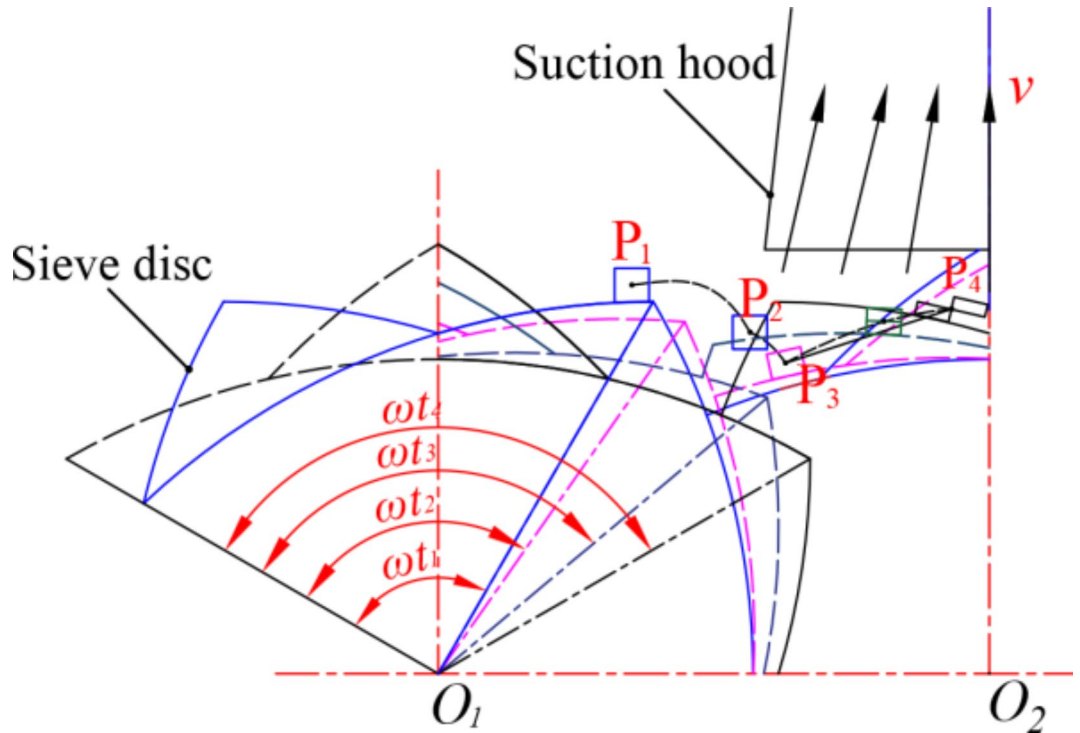


**Fig. 4.** Analysis of the whole motion process of the film and impurity materials separation. The simplified structure of the sieve disc is represented by arcs, and the arcs of different colors represent different positions of the sieve disc after rotation. The linear frame is used to represent the simplified structure of the suction hood, and the linear arrow represents the direction of the airflow. The connection curve between adjacent points of  $P_1, P_2, P_3$  and  $P_4$  is the trajectory of the material. Note:  $v$  is the air velocity, m/s;  $\omega$  is the angular velocity of the sieve disc, rad/s;  $t_1$  is the time it takes for the film and impurity materials to move to the point  $P_1$ , s;  $t_2$  is the time it takes for the material to move to the point  $P_3$ , s;  $t_3$  is the time spent on the movement of the material from point  $P_3$  to point  $P_4$ , s;  $t_4$  is the time it takes for the material to move to the point  $P_4$ , s.

third law and elastic wave theory<sup>25</sup>, the force  $F_{ms}$  that the materials are subjected to from the sieve disc is expressed by Eq. (10).

$$F_{ms} = \frac{2mg \cos \sigma - k\rho_0 S v^2 \sin(\beta - \sigma)}{2\delta} h, (0 \leq h \leq \delta) \quad (10)$$

where,  $h$  is the deformation of the material when it collides with the sieve disc, m.

Equation (11) expresses the kinetic energy change after the collision (deformation energy  $\Delta E$ ).

$$\begin{cases} \Delta E = \int_0^\delta \frac{F_{ms}^2}{2ES'} dh = \frac{[2mg \cos \sigma - k\rho_0 S v^2 \sin(\beta - \sigma)]^2 \delta}{24ES'} \\ S' = L_1 B, [id + i\Delta d \leq B \leq id + (i + 1)\Delta d] \end{cases} \quad (11)$$

where,  $E$  is the modulus of elasticity of the film and impurity materials;  $S'$  is the contact area of the material with the sieve discs,  $m^2$ ;  $B$  is the contact length of the material with the sieve discs in the width direction, m;  $i$  is the number of sieve discs contacted by the material, pcs;  $d$  is the thickness of the sieve discs, m;  $\Delta d$  is the gap between the sieve discs, m.

The velocity  $v_3$  of the film-impurity material after colliding with the sieve disc can be expressed by Eq. (12).

$$v_3 = \sqrt{v_2^2 - \frac{[2mg \cos \sigma - k\rho_0 S v^2 \sin(\beta - \sigma)]^2 \delta}{12mES'}} \quad (12)$$

(4) The relative slipping of cotton straw, soil and residual film ( $P_3 \sim P_4$  stage).

After the collision, the film and impurity materials continue to move along the sieve disc, and the internal components of the residual film, cotton straw and soil maintain their relative slipping until they are separated. The spatial distributions of the film and impurity material components are more complex. To simplify the

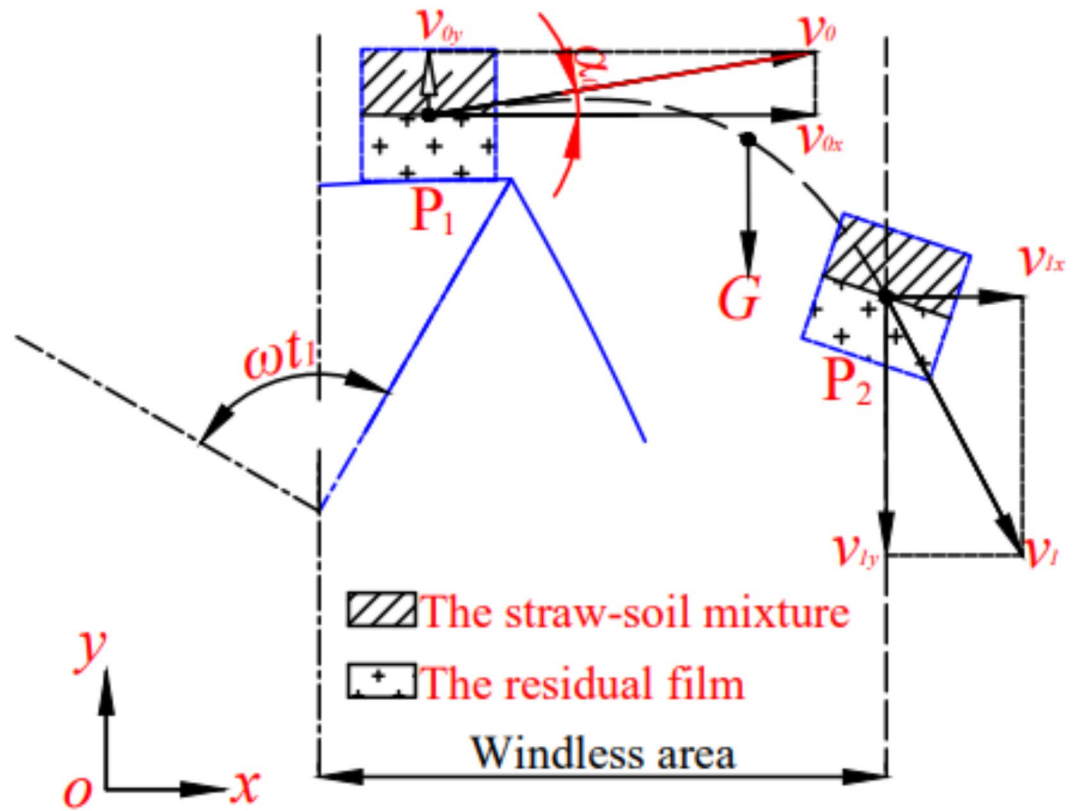


**Fig. 5.** Force analysis of the throwing process in the windless area ( $P_1 \sim P_2$  stage). It contains a process of oblique throwing. Note:  $v_0$  is the initial velocity of the material at point  $P_1$ , with the horizontal component  $v_{0x}$  and the vertical component  $v_{0y}$ , m/s;  $\alpha_0$  is the angle between the projection direction and the horizontal plane, °;  $v_1$  is the velocity after the movement of  $t_1$  time, with the horizontal component  $v_{1x}$  and the vertical component  $v_{1y}$ , m/s;  $G$  is the gravity of the material, N.

analysis, the cotton straw and soil are regarded as a whole, named straw-soil mixture, and the film and impurity materials are regarded as a mixture of residual films and straw-soil mixture. The distribution of the straw-soil mixture in the upper layer and the residual films in the lower layer is studied. It is assumed that the displacement of the film and impurity materials on the sieve disc is a straight line during the time interval from  $t_3$  to  $t_4$ .

The partial velocity  $v_{3q}$  of  $v_3$  in the tangential direction of the contact point and the linear velocity  $v_s$  of the sieve disc at the point of contact are illustrated by Eq. (13).

$$\begin{cases} v_{3q} = v_3 \cos(\alpha_1 + \sigma) \\ v_s = \omega r \\ \omega = \frac{\pi n}{30} \end{cases} \quad (13)$$

where,  $n$  is the rotational velocity of the disc sieve, r/min.

Figure 8 shows the force analysis of the whole material, and Fig. 9 presents the force analysis of material component. As shown in Figs. 8 and 9, if  $v_{3q} > v_s$ , the film and impurity materials tend to slip to the right relative to the sieve disc, so the friction direction is the opposite (to the left), and the material performs deceleration motion. Conversely, if  $v_{3q} < v_s$ , the slipping trend of the material is to the left, the friction direction is to the right, and the material undergoes accelerated motion.

As shown in Fig. 8, the material is in force equilibrium in the normal direction at the point of contact with the sieve disc. Equation (14) gives the force balance equation in the normal direction of the whole material.

$$\begin{cases} F_N + \frac{k\rho_0 S v^2}{2} \sin(\beta + \sigma) + m\omega^2 r \sin(\theta - \sigma) = mg \cos \sigma \\ F_r = m\omega^2 r \end{cases} \quad (14)$$

The straw-soil mixture and residual films are isolated and analyzed separately in terms of force as shown in Fig. 9. When the straw-soil mixture and residual films are subjected to the wind force, their windward areas and the forces exerted by the airflow are different.

When analyzing the windward area of the straw-soil mixture, the following assumptions are made: (1)  $n'$  cotton straws and  $n''$  soil particles are laid flat in the upper layer of residual films; (2) cotton straws are assumed to be straight cylinders with uniform moisture content and diameter in all parts, and their windward area is a

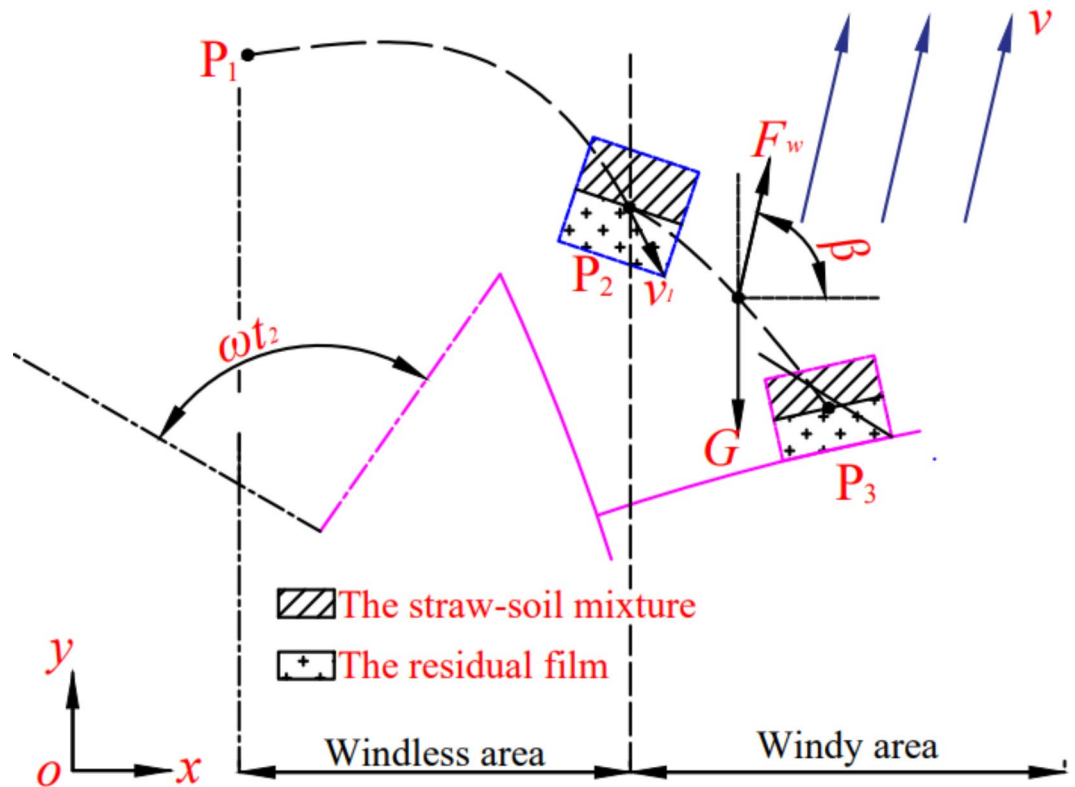


**Fig. 6.** Force analysis of the throwing process in windy area. Under the action of airflow, the oblique throwing trajectory of the material changes, and the falling point of the material on the sieve surface is located on the second disc. Note:  $F_w$  is the wind force of the film and impurity materials,  $N$ ;  $\beta$  is the angle between  $F_w$  and the  $x$ -axis,  $^\circ$ .

rectangular projection area at the level of the cylindrical axis; and (3) soil particles are assumed to be equal-diameter spheres that do not disintegrate under the action of the airflow, and their windward area is a circular area with the same radius as the sphere. The force balance equations in the normal direction of the segmental material are signified by Eq. (15).

$$\begin{cases} F_{N1} + \frac{k\rho_0 S_1 v^2}{4} \sin(\beta + \sigma) + m_1 \omega^2 r + \Delta h \sin(\theta - \sigma) = m_1 g \cos \sigma \\ F_N + \frac{k\rho_0 S_2 v^2}{4} \sin(\beta + \sigma) + m_2 \omega^2 r \sin(\theta - \sigma) = m_2 g \cos \sigma + F_{N2} \\ S_1 = n' d_1 l_1 + n'' \pi r_1^2 \\ S_2 = L_1 L_2 \end{cases} \quad (15)$$

where,  $S_1$  is the windward area of the mixture,  $m^2$ ;  $m_1$  is the mass of the mixture,  $kg$ ;  $\Delta h$  is the thickness of the residual film material layer,  $m$ ;  $S_2$  is the windward area of the residual film material layer,  $m^2$ ;  $m_2$  is the mass of the residual films,  $kg$ ;  $d_1$  is the average diameter of cotton straws,  $m$ .  $l_1$  is the average length of cotton straws,  $m$ ;  $r_1$  is the average radius of soil particles,  $m$ .

From the geometric relationship in Fig. 10, there is a relationship shown in Eq. (16) among the key structural parameters of the sieve disc.

$$\begin{cases} \sigma = \omega t - \varepsilon' \\ \theta = \omega t - \varepsilon + \frac{\pi}{2} \\ r \sin \varepsilon = R \sin \varepsilon' \\ r = \frac{\sqrt{3}}{3} R \left( \sqrt{(\cos \varepsilon)^2 + 2 - \cos \varepsilon} \right) \end{cases} \quad (16)$$

When the relative movement trend of the material is to the right, the resultant force of the wind force  $F_{w1}$ , inertia force  $F_{r1}$ , gravity  $G_1$  and friction  $f_1$  in the normal direction provides acceleration for the straw-soil mixture, and the resultant force of the wind force  $F_{w2}$ , inertia force  $F_{r2}$ , gravity  $G_2$ , friction  $f_2$  and friction  $f$  in the normal direction provides acceleration for the residual films. The motion models of the straw-soil mixture and residual films, as shown in Eq. (17), are obtained as follows.

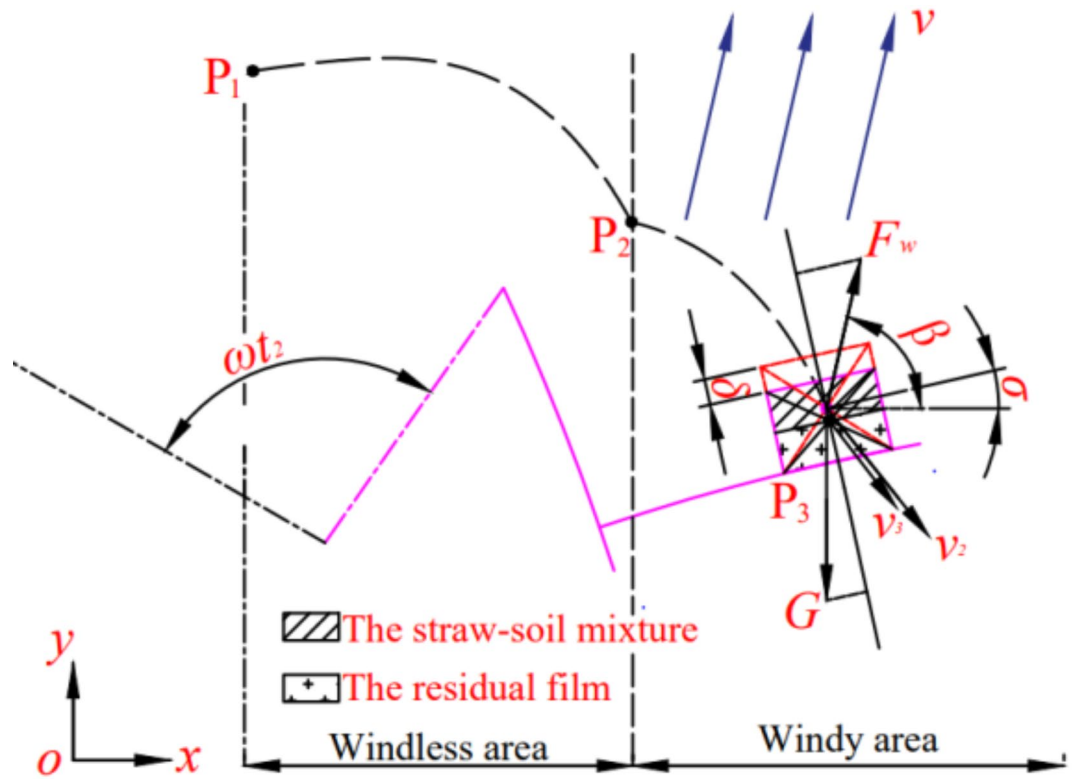


**Fig. 7.** Force analysis of the collision stage. It contains the process of the mixture material's deformation. Note:  $v_2$  is the velocity of the material after the movement of  $t_1$  time, m/s;  $v_3$  is the velocity of the material after collision with the sieve disc, m/s;  $\sigma$  is the angle between the tangent direction of the contact point and the  $x$ -axis, °;  $\delta$  is the maximum deformation amount of the material when it collides with the sieve disc, m.

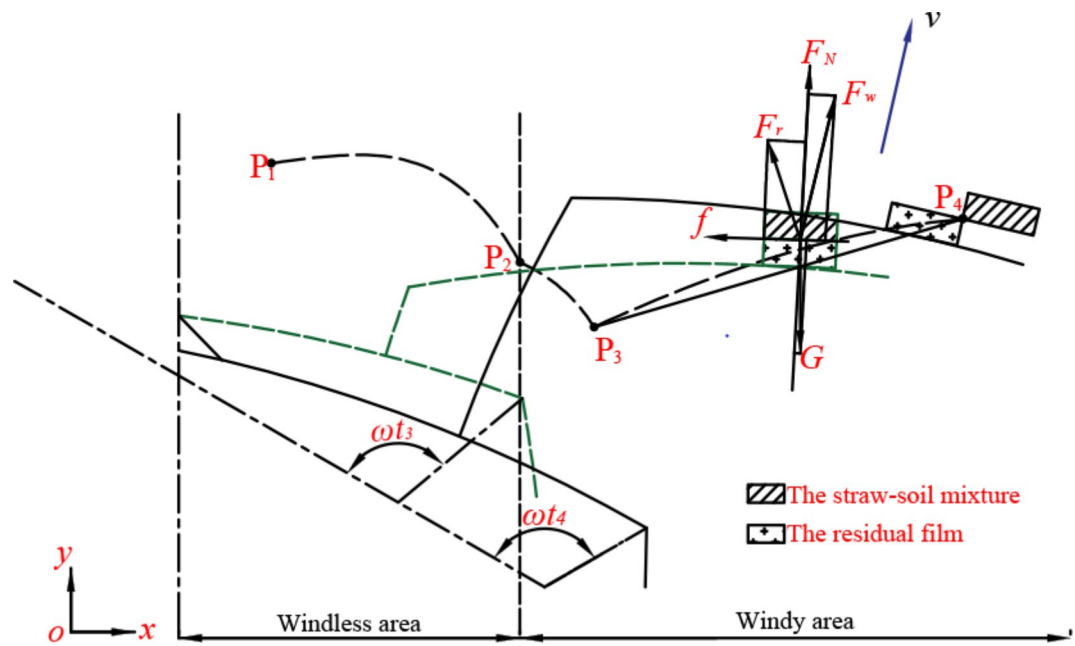


**Fig. 8.** Force analysis of the whole material. The friction force and airflow force play a major role, and the relative displacement between the components of the mixture is generated. Note:  $F_N$  is the support force of the sieve disc on the material, N;  $F_r$  is the inertial centrifugal force of the integral material on the sieve disc, N;  $f$  is the friction force of the sieve disc to the integral material, N.

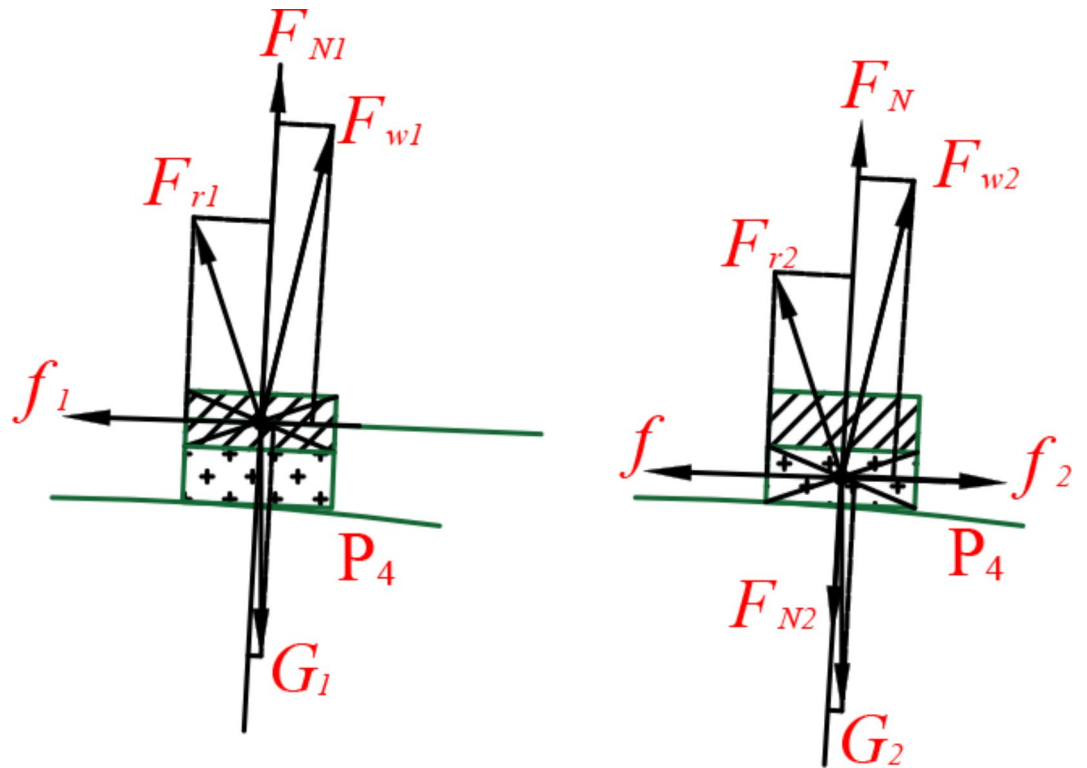


**Fig. 9.** Force analysis of material components. Note:  $F_{N1}$  is the support force of the residual films on the straw-soil mixture, N;  $F_{r1}$  is the inertial centrifugal force of the straw-soil mixture on the residual film layers, N;  $F_{w1}$  is the wind force of the straw-soil mixture, N;  $f_1$  is the friction force of the residual films to the straw-soil mixture, N;  $G_1$  is the gravity of the straw-soil mixture, N;  $F_{N2}$  is the pressure on the residual films from the straw-soil mixture, N;  $F_{r2}$  is the inertial centrifugal force of the residual films on the sieve disc, N;  $F_{w2}$  is the wind force of the residual films, N;  $f_2$  is the friction force of the straw-soil mixture to the residual films, N;  $G_2$  is the gravity of the residual films, N.  $F_{N1}$  and  $F_{N2}$  are a pair of action and reaction forces, which are equal in size and opposite in direction.

$$\left\{ \begin{array}{l} m_1 \frac{dv_4}{dt} = \mu_1 \left[ m_1 g \cos \sigma - \frac{k\rho_0 S_1 v^2}{4} \sin(\beta + \sigma) - m_1 \omega^2 (r + \Delta h) \sin(\theta - \sigma) \right] \\ + m_1 \omega^2 (r + \Delta h) \cos(\theta - \sigma) - \frac{k\rho_0 S_1 v^2}{4} \cos(\beta + \sigma) - m_1 g \sin \sigma \\ m_2 \frac{dv'_4}{dt} = \mu \left\{ \begin{array}{l} m_2 g \cos \sigma + m_1 g \cos \sigma - \frac{k\rho_0 S_1 v^2}{4} \sin(\beta + \sigma) \\ - m_1 \omega^2 (r + \Delta h) \sin(\theta - \sigma) - m_2 \omega^2 r \sin(\theta - \sigma) - \frac{k\rho_0 S_2 v^2}{4} \sin(\beta + \sigma) \end{array} \right\} \\ - \mu_1 \left[ m_1 g \cos \sigma - \frac{k\rho_0 S_1 v^2}{4} \sin(\beta + \sigma) - m_1 \omega^2 (r + \Delta h) \sin(\theta - \sigma) \right] \\ + m_2 \omega^2 r \cos(\theta - \sigma) - \frac{k\rho_0 S_2 v^2}{4} \cos(\beta + \sigma) - m_2 g \sin \sigma \end{array} \right. \quad (17)$$

Where,  $v_4$  is the velocity of the straw-soil mixture after the movement of  $t_4$  time, m/s;  $\mu_1$  is the friction coefficient between the straw-soil mixture and the residual films;  $v'_4$  is the velocity of the residual films after the movement of  $t_4$  time, m/s;  $\mu$  is the friction coefficient between the residual films and the sieve disc.

The initial conditions are as follows: when  $t_3 = 0$ ,  $X_4 = 0$ ,  $X'_4 = 0$ , and  $v_{40} = v_{3q}$ , Eqs. (18) and (19) represent the first-order and the second-order integrals of Equations (17).

$$\left\{ \begin{array}{l} v_4 = \frac{g}{\omega} (\mu_1 \sin \sigma + \cos \sigma) - \frac{k\rho_0 S_1 v^2}{4\omega m_1} [\sin(\beta + \sigma) - \mu_1 \cos(\beta + \sigma)] \\ - \omega^2 (r + \Delta h) [\mu_1 \sin(\theta - \sigma) - \cos(\theta - \sigma)] t_4 + v_{3q} \\ v'_4 = \frac{g}{\omega} (\mu \sin \sigma + \cos \sigma) - \frac{k\rho_0 S_2 v^2}{4\omega m_2} [\sin(\beta + \sigma) - \mu \cos(\beta + \sigma)] \\ - \omega^2 r [\mu \sin(\theta - \sigma) - \cos(\theta - \sigma)] t_4 + (\mu - \mu_1) \left( \frac{m_1}{m_2} \right) \frac{g}{\omega} \cos \sigma \\ + (\mu - \mu_1) \frac{k\rho_0 S_1 v^2}{4\omega m_2} \cos(\beta + \sigma) - (\mu - \mu_1) \left( \frac{m_1}{m_2} \right) \omega^2 (r + \Delta h) \sin(\theta - \sigma) t_4 + v_{3q} \end{array} \right. \quad (18)$$



$$\begin{aligned} \Delta X = & \frac{k\rho_0 v^2}{4\omega^2} \left[ \cos(\beta + \sigma) \left( \frac{S_2}{m_2} - \frac{S_1}{m_1} \right) + \sin(\beta + \sigma) \frac{\mu m_1(S_1 + S_2) - \mu_1 S_1(m_1 + m_2)}{m_1 m_2} \right] \\ & - \frac{1}{2} \omega^2 \Delta h \cos(\theta - \sigma) t^2 + (\mu_1 - \mu) \frac{g}{\omega^2} \left[ \cos \sigma - \left( \frac{m_1}{m_2} \right) \sin \sigma \right] \\ & + \frac{1}{2} \omega^2 \sin(\theta - \sigma) t^2 \left[ \frac{\mu_1(m_1 + m_2)(r + \Delta h) - \mu m_1(r + \Delta h) - \mu m_2 r}{m_2} \right] > L_1 \end{aligned} \quad (21)$$

Similarly, the critical condition for complete separation when the relative movement trend of the material is to the left is obtained, as shown in Eq. (22).

$$\begin{aligned} \Delta X = & \frac{k\rho_0 v^2}{4\omega^2} \left[ \cos(\beta + \sigma) \left( \frac{S_1}{m_1} - \frac{S_2}{m_2} \right) + \sin(\beta + \sigma) \frac{\mu m_1(S_1 + S_2) - \mu_1 S_1(m_1 + m_2)}{m_1 m_2} \right] \\ & - \frac{1}{2} \omega^2 \Delta h \cos(\theta - \sigma) t^2 + (\mu_1 - \mu) \frac{g}{\omega^2} \left[ \cos \sigma - \left( \frac{m_1}{m_2} \right) \sin \sigma \right] \\ & + \frac{1}{2} \omega^2 \sin(\theta - \sigma) t^2 \left[ \frac{\mu_1(m_1 + m_2)(r + \Delta h) - \mu m_1(r + \Delta h) - \mu m_2 r}{m_2} \right] > L_1 \end{aligned} \quad (22)$$

From the above analysis, before contacting the sieve disc, the motion states of the film and impurity materials in the windless area are affected by the initial velocity, throwing angle and other factors. In the windy area, the motion state is affected by mass, airflow velocity, windward area and other factors. In the collision stage, the motion state is affected by mass, airflow velocity, contact area with the sieve disc, compression amount of the material and other factors. In the relative motion of cotton straw, soil and residual film to the separation stage, the motion state is affected by the mass, disc rotational velocity, sieve disc structure size, airflow velocity, windward area, friction coefficient, residual film material layer thickness and other factors. The mass of the material is related to the feeding quantity. The windward area, compression amount of the material and residual film material layer thickness are related to the spatial distribution of internal components. The contact area is related to the disc sieve working width. The friction coefficient is related to the material properties. When the proportion and spatial distribution of the internal components and the structure size of the device are fixed, the material movement state is mainly related to the parameters such as feeding quantity, airflow velocity and disc rotational velocity. The airflow velocity is mainly affected by the fan rotational velocity. Therefore, the relationship between the airflow velocity and fan rotational velocity is further explored.

## Materials and methods

### Simulation of airflow-disc sieve double action flow field

The airflow-rotating disc film impurity separation device is based on the differences in the aerodynamic characteristics of the residual film, cotton straw and soil, and the turbulence generated by the fan is used to separate the mixed materials. Through Fluent flow field simulation, the distribution law of the airflow field in the double action area of the device is investigated, and the influence of different fan rotational velocities on the airflow velocity of the sieve surface is analyzed. Different wind pressure parameters are used to characterize the different fan rotational velocities.

Based on the structural dimensions of the device, SolidWorks 2022 software is used to establish a three-dimensional model of the double action region. The model is saved in IGES format and then imported into ICFEM software for fluid domain extraction and meshing. A tetrahedral unstructured mesh with high precision is adopted. The connection port between the suction hood and pipeline is set as the pressure outlet of the model, and the discharge port below the disc sieve is set as the pressure inlet. The standard  $k-\varepsilon$  turbulence model and simple algorithm are adopted<sup>26</sup>. The initial wind pressure parameter of the pressure outlet is set to -100 Pa, and the other wind pressure parameters are set to -50 Pa, -75 Pa, -125 Pa and -150 Pa, respectively. By analyzing the simulation results, the most suitable wind pressure for the film and impurity materials separation is obtained, and the airflow velocity of the connection port between the suction hood and pipeline under the wind pressure is recorded.

After analyzing the results, a matching experiment between the wind pressure and fan rotational velocity is carried out. The frequency converter controls the fan rotational velocity of the separation device. The airflow velocity of the connection port between the suction hood and the pipeline is measured 5 times by a thermal airflow velocity anemometer (Model: Hima AR866A; Accuracy: 0.01 m/s; Manufacturer: Dongguan Wanchuang Electronic Products Co., Ltd.). The value of each measurement is recorded and the average value of the 5 measurements is obtained. The frequency converter is continuously adjusted to change the fan rotational velocity until the error between the average value and the simulated airflow velocity is less than 5%. The current fan rotational velocity is recorded, which provides the data basis for the experiment of separation performance.

### Experiment of the separation performance

#### Experimental conditions and equipment

In July 2022, the experiment of the film and impurity materials separation performance was carried out in the equipment debugging room of Ruiyida Machinery Equipment Co., Ltd., Shihezi Development Zone, Shihezi City, Xinjiang Uygur Autonomous Region. Figure 11 shows the constructed airflow-disc sieve type film separation test bench.



**Fig. 11.** Airflow-disc sieve type film separation test bench.

The experimental material was the crushed film and impurity materials after the bundle crushing device jointly developed by Xinjiang Academy of Agricultural Reclamation Sciences, Shihezi Development Zone Ruiyida Machinery Equipment Co., Ltd., and Shihezi University. The maximum profile size of the experimental material was less than 400 mm, and the maximum profile size in the range of (0,100] mm accounted for less than 15%. The average impurity content in the experimental material was 81.09%.

The main instruments and equipment for the experiment include a bench scale (Model: HLT-908; Accuracy: 1 g, Manufacturer: Huaritai Electronic Scale Co., Ltd.), hand-held tachometer (Accuracy:  $\pm 1\%$ , Manufacturer: Shanghai Tachometer Factory) and plastic bags.

#### *Experimental scheme*

Based on the pre-experiment, fan rotational velocity  $A$  (870 ~ 1450 r/min), disc rotational velocity  $B$  (26 ~ 54 r/min) and feeding quantity  $C$  (110 ~ 198 kg/h) were determined as the experimental factors. The impurity removal rate  $Y_1$  and film leakage rate  $Y_2$  were used as evaluation indexes for the separation performance of the device.

#### (1) Impurity removal rate $Y_1$ .

The residual films were sorted and washed from the residual film collection box after separation. The rate of impurities in the separated films is the total mass of the material in the box minus the mass of the washed films, and then with the total mass of the material in the box ratio. Equation (23) gives the definition of the rate of impurities in the separated films.

$$y = \frac{M_j - m_c}{M_j} \times 100\% \quad (23)$$

where,  $y$  is the rate of impurities in the separated films, %;  $M_j$  is the total mass of the material in the residual film collection box, kg;  $m_c$  is the mass of the washed films, kg.

The impurity removal rate is the total impurity mass of the experimental material minus the impurity mass of the material in the residual film collection box, and then with the total impurity mass of the experimental material ratio. Equation (24) gives the definition of the impurity removal rate  $Y_1$ .

$$Y_1 = \frac{M \times s - M_j \times y}{M \times s} \times 100\% \quad (24)$$

where,  $Y_1$  is the impurity removal rate, %;  $M$  is the total mass of the experimental material, kg;  $s$  is the average impurity content of the experimental material, %.

## (2) Film leakage rate $Y_2$ .

The film leakage rate is the total residual film mass of the experimental material minus the mass of the washed films in the residual film collection box, and then with the total residual film mass of the experimental material ratio. Equation (25) gives the definition of the film leakage rate  $Y_2$ .

$$Y_2 = \frac{M \times (1 - s) - M_j \times (1 - y)}{M \times (1 - s)} \times 100\% \quad (25)$$

where,  $Y_2$  is the film leakage rate, %.

The experiment was conducted using three-factor and three-level Box-Behnken response surface analysis, and Table 2 presents the factor level taking and coding table. A total of 17 groups of experiments were conducted, each group was repeated 5 times, and the average was taken as the result. Design-Expert 13 software was used for the experimental scheme and analysis of the results.

### Experimental steps

First, the experimental materials were randomly grabbed and evenly laid on the feeding conveyor. Then, the power supply of the test bench was connected, and the fan rotational velocity and disc rotational velocity were set by the frequency converter. When the separation device was running stably, the feeding conveyor and elevator were started, and the materials were transported to the disc sieve. When all materials passed through the sieve surface, the power supply was turned off, and the materials in the residual film collection box were weighed, sorted and recorded.

## Results and discussion

### Results of simulation

#### Analysis of the initial model simulation

Figures 12 and 13 respectively depict the airflow velocity distribution cloud diagram and velocity vector diagram of the suction hood width direction neutral surface.

As shown in Figs. 12 and 13, the airflow generated by the fan mainly affects the movement of the film and impurity materials on the sieve disc directly below the suction hood. Before entering the suction hood (I), the airflow is distributed along the edge of the sieve disc, forming a low-velocity region. In this region, the velocity is greater than the suspension velocity of the residual film but less than that of the cotton straw and soil, so that the films tend to enter the suction hood. When the airflow enters the suction hood along the edge of the disc (II), an accelerated region is formed. This is due to the decrease in the airflow movement space formed by the sieve disc and suction hood, forming a 'throat tube', which contributes to the rapid stratification and separation of the materials. In this region, the residual films quickly concentrate on the upper layer of the film and impurity materials and enter the suction hood. After the airflow enters the suction hood (III), two micro-velocity regions are formed at 1/3 of the two edges of the suction hood near the bottom. This is because the airflow through the 'throat tube' still has an accelerating trend, converging towards the middle of the suction hood. The airflow in the middle area of the suction hood accelerates upward. This is because the hood has a wide lower and narrow upper structure, resulting in a continuous decrease in the airflow movement space and increasing acceleration of the airflow. From bottom to top, an airflow belt with a velocity level higher than the level is formed, which promotes the residual films to pass through the hood quickly without blockage.

To further analyze the variation law of the airflow velocity on the sieve surface under the double action, the distribution of airflow velocity measurement points was established as shown in Fig. 14. Furthermore, Fig. 14a shows 11 measurement point columns such as A~A' established in the length direction of the sieve surface, and Fig. 14b illustrates the distribution of 29 measurement points in the width direction of each measurement point column. Thus, a total of 319 measurement points is taken.

Through the CFD-Post module, the airflow velocity at each measuring point is extracted when the wind pressure is -100 Pa, and the change trend of airflow velocity is obtained, as shown in Fig. 15. The change law of airflow velocity at symmetrical positions on both sides of the middle line (column 6) is consistent, which is manifested as the periodic fluctuation of airflow velocity from columns 2 to 10, and the overall change law is approximately 'jagged'. Among them, the airflow velocity near the edge of the suction hood (columns 2 and 10 as one group, columns 3 and 9 as another group) shows a periodic fluctuation that first attenuates and then increases in the width direction of the disc sieve, and the velocity trend near the center (columns 4~8) is the

Level	Fan rotational velocity A/(r·min <sup>-1</sup> )	Disc rotational velocity B/(r·min <sup>-1</sup> )	Feeding quantity C/(kg·h <sup>-1</sup> )
-1	870	26	110
0	1160	40	154
1	1450	54	198

**Table 2.** Factor level taking and coding table for Box-Behnken experiment.

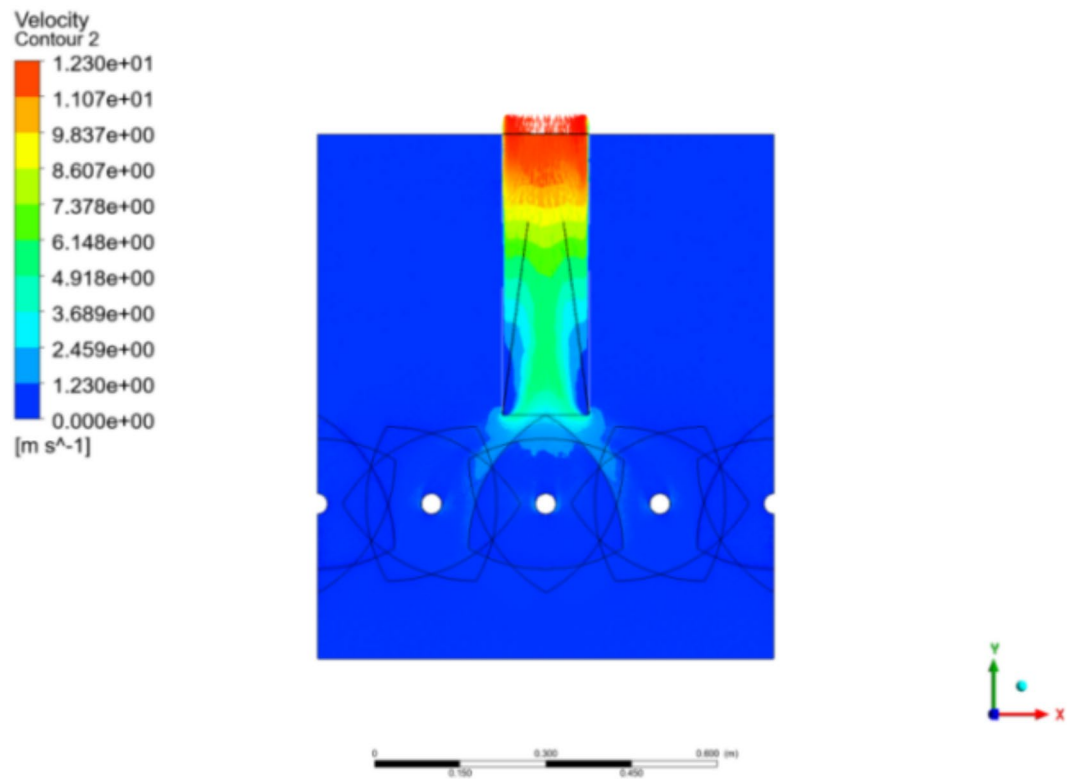


**Fig. 12.** Airflow velocity distribution cloud. The main variation range of the airflow is 1.23 m/s to 12.30 m/s.

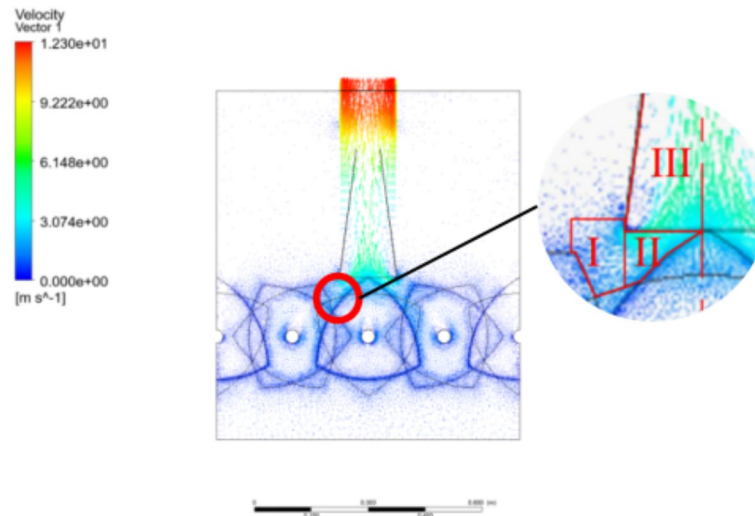


**Fig. 13.** Vector diagram of air velocity distribution. Note: I represents the stage before the airflow enters the suction hood; II represents the stage of airflow entering the suction hood; III represents the stage after the airflow enters the suction hood.

opposite. This is because the adjacent discs on the same shaft are arranged at a phase angle of  $60^\circ$ , and the adjacent discs on the adjacent shaft are staggered at a phase angle of  $30^\circ$ , thus, different airflow motion spaces are formed in the cross-section of each column of the measuring points (Fig. 14b). The corresponding airflow motion space changes periodically, and the airflow velocity also fluctuates periodically. The law is that the airflow velocity near the sieve disc is small, and the velocity far from the disc is large. This is due to the negative pressure field formed by the fan and suction hood. Under negative pressure, the airflow in the external flow field passes through the sieve discs and enters the suction hood from the bottom of the disc sieve. When the airflow bypasses the disc, the streamline turns inward (Fig. 16), and there is a reverse pressure gradient. The kinetic energy of

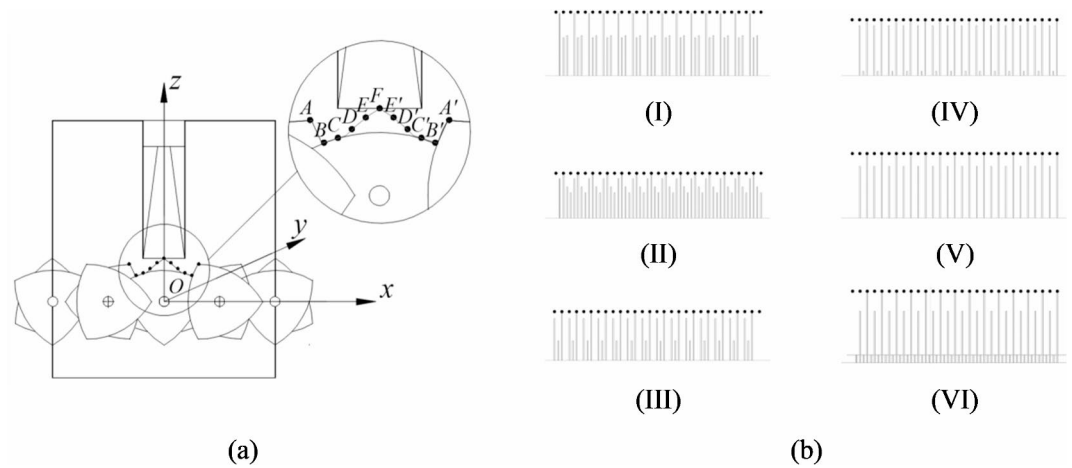


**Fig. 14.** Distribution of airflow velocity measurement points in the airflow-disc sieve double action area. (a) Measuring points along the length of the disc sieve. A~A' represent Column 1~Column 11 in sequence. (b) Measuring points along the width of the disc sieve. (I) represents Column 1 (also Column 11); (II) represents Column 2 (also Column 10); (III) represents Column 3 (also Column 9); (IV) represents Column 4 (also Column 8); (V) represents Column 5 (also Column 7); (VI) represents Column 6.

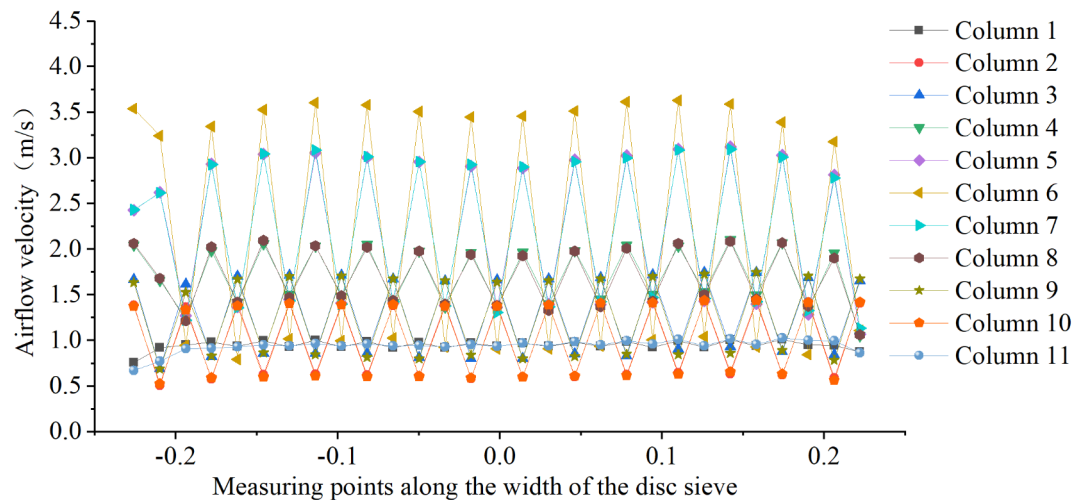


**Fig. 15.** Trend of airflow velocity on the sieve surface of the initial model.

air is converted into pressure energy, and the velocity decreases. After passing through the discs, the velocity increases under the action of the fan and the suction hood. Therefore, the airflow velocity near the discs is in the decreasing stage, and the velocity far from the discs is in the continuous acceleration stage, which makes the transverse airflow of the sieve surface always fluctuate. The airflow velocity difference aggravates the disturbance of the migration trajectory of the material on the sieve surface, which is beneficial to the movement of the residual films in the lower layer to the upper layer, and then realizes separation under airflow attraction. The airflow velocity of the sieve surface (columns 1 and 11) away from the suction hood is basically stable, and the average velocity is 0.95 m/s. This is because there is no obstacle near the measuring point, which has no effect on the airflow motion space.

#### *Analysis of the effect of wind pressure on airflow velocity*

Figure 17 presents the trends of the airflow velocity on the sieve surface under different wind pressure conditions. Figure 17a, b, c and d represent the variation trends at the air inlet under  $-50$  Pa,  $-75$  Pa,  $-125$  Pa, and  $-150$  Pa wind pressure, the overall trends being basically the same. With the increase in wind pressure, the airflow velocity increases, but the growth rate gradually decreases, indicating that the wind pressure has a significant effect on the airflow velocity. When the negative wind pressure increases from 50 to 150 Pa, the growth rate of the airflow velocity near the discs decreases from 22.67 to 9.61%, and that of the velocity far from the discs decreases from 27.80 to 11.58%. This shows that when the negative wind pressure continues to increase to a critical value, the airflow velocity tends to be stable. During the separation process, the airflow velocity on the sieve surface

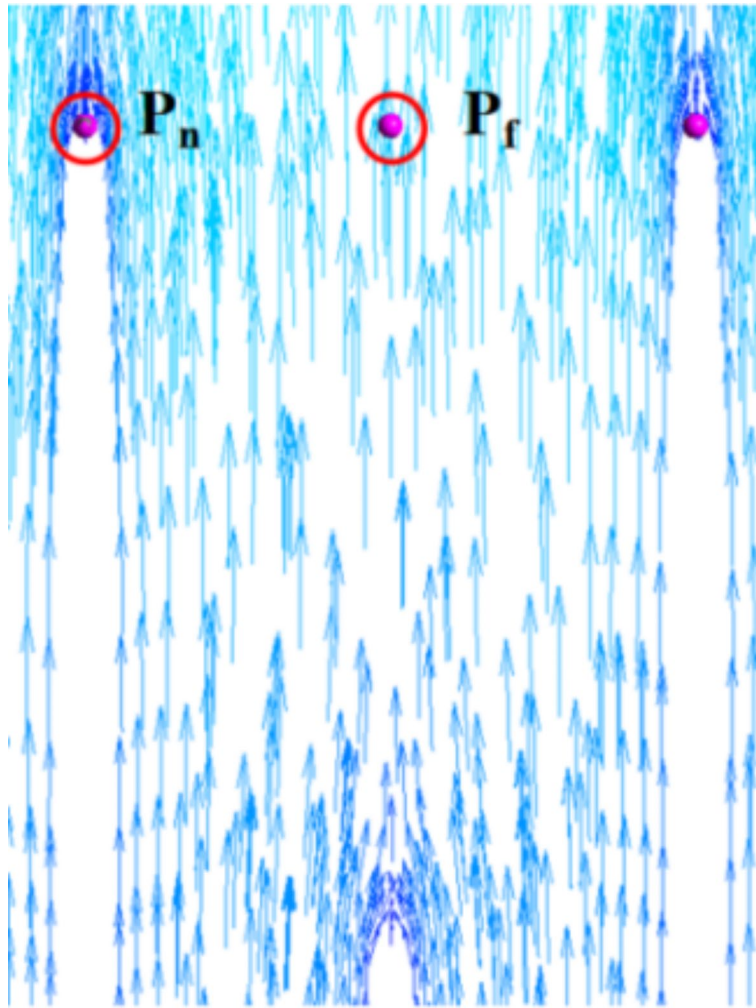


**Fig. 16.** Airflow distribution around the measurement points.  $P_n$  refers to the measuring point near the sieve disc;  $P_f$  refers to the measuring point far from the sieve disc.

needs to be between the suspension velocity of the residual film and that of impurities such as cotton straw and soil. The maximum airflow velocity cannot exceed the suspension velocities of cotton straw and soil, and the minimum airflow velocity cannot be smaller than the suspension velocity of the residual film. In the previous experiments, the suspension velocity range of the residual film was 1.04 ~ 3.20 m/s, the suspension velocity range of the cotton straw was 6.70 ~ 8.59 m/s, and the suspension velocity range of the soil was 6.40 ~ 15.80 m/s. When the wind pressure is -125 Pa, the maximum velocity far from the discs is 3.57 m/s, and the minimum is 1.57 m/s, which are higher than the suspension velocity of the residual film, which can make the residual films at the measuring point on the far screen surface separate from the cotton stalks and stones under the action of airflow. When the wind pressure is -125 Pa, the airflow velocity far from the discs has covered the range of the residual film suspension velocity, and the utilization rate of the airflow is high, which meets the airflow demand during the separation process. Under this condition, the airflow velocity of the connection port between the suction hood and pipeline is 13.67 m/s.

When the fan rotational velocity is 1160 r/min, the average value of the airflow velocity of the connection port between the suction hood and pipeline is 13.15 m/s, and the error with the airflow velocity value under the wind pressure of -125 Pa in the simulation test is 3.80% (less than 5%), which provides a basis for the setting of the fan rotational velocity in the film and impurity materials separation experiment.

## Results of separation experiment

### *Regression analysis of experiment results*

Table 3 showcases the Box-Behnken experimental design and results, unveiling how fan rotational velocity  $A$ , disc rotational velocity  $B$ , feeding quantity  $C$  influence impurity removal rate  $Y_1$  and film leakage rate  $Y_2$ . According to Table 3, Design-Expert 13 data analysis software was used for multiple regression fitting analysis. A variance analysis was conducted on the experimental results and regression models, and the results are shown in Table 4. Coded regression models with the impurity removal rate  $Y_1$  and the film leakage rate  $Y_2$  as response functions and the influencing factors as independent variables were obtained, as shown in Eq. (26).

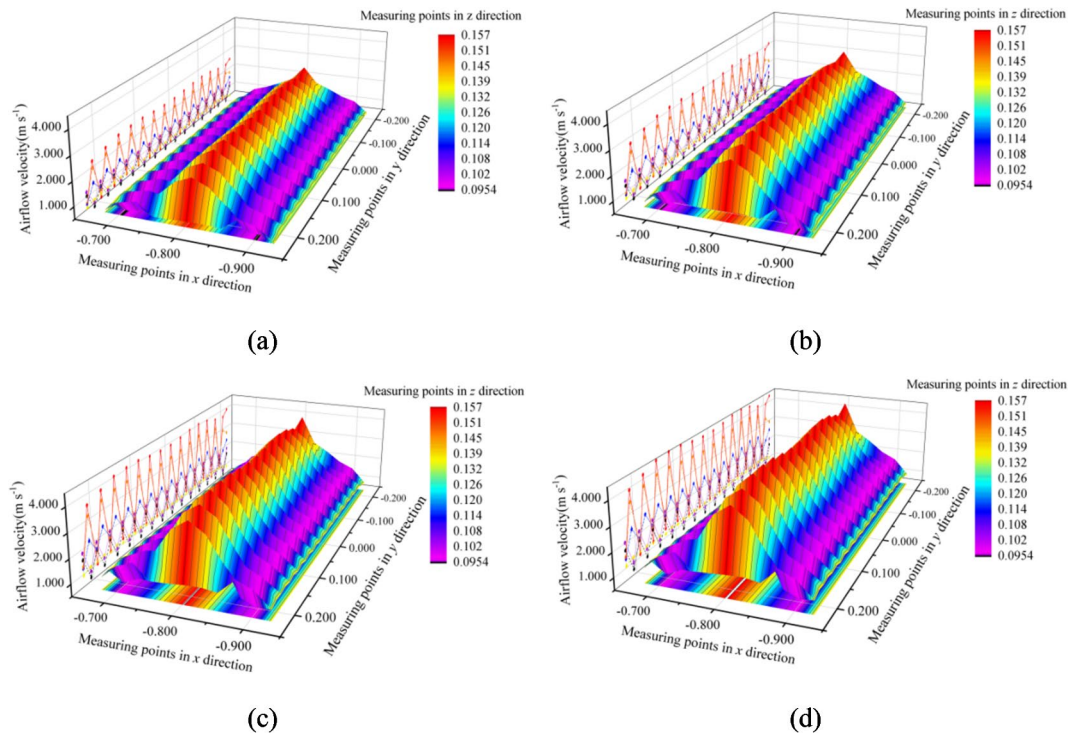


**Fig. 17.** Trend of airflow velocity on screen surface under different wind pressure conditions, plotted by Origin 2018 software (<https://www.originlab.com/>). (a) Wind pressure is -50 Pa; (b) wind pressure is -75 Pa; (c) wind pressure is -125 Pa; (d) wind pressure is -150 Pa.

No	Experimental factors and levels			Response indicators	
	Fan rotational velocity $A/(r\cdot\text{min}^{-1})$	Disc rotational velocity $B/(r\cdot\text{min}^{-1})$	Feeding quantity $C/(\text{kg}\cdot\text{h}^{-1})$	Impurity removal rate $Y_1$ (%)	Film leakage rate $Y_2$ (%)
1	0	0	0	94.50	38.11
2	0	1	-1	95.46	51.12
3	0	0	0	95.10	40.26
4	0	0	0	94.69	38.72
5	1	-1	0	90.07	23.63
6	-1	-1	0	96.81	26.46
7	1	1	0	96.07	20.62
8	0	0	0	96.35	33.32
9	-1	0	-1	95.73	48.15
10	-1	1	0	94.16	44.82
11	0	1	1	93.36	45.47
12	1	0	-1	94.84	26.41
13	0	-1	-1	95.28	39.33
14	-1	0	1	94.11	44.87
15	0	0	0	94.84	39.27
16	0	-1	1	93.45	30.26
17	1	0	1	92.32	35.80

**Table 3.** Box-Behnken experimental design and results: unveiling how  $A$ ,  $B$ ,  $C$  influence  $Y_1$  and  $Y_2$ .

Sources	Impurity removal rate $Y_1$		Film leakage rate $Y_2$	
	F	P	F	P
Model	7.23	0.0081**	8.93	0.0043**
A	12.13	0.0102*	28.67	0.0011**
B	2.54	0.1547	15.37	0.0057**
C	14.00	0.0072**	0.6352	0.4516
AB	32.17	0.0008**	7.83	0.0266*
AC	0.3483	0.5736	2.75	0.1412
BC	0.0313	0.8645	0.2004	0.6679
$A^2$	1.65	0.2392	10.03	0.0158
$B^2$	0.8396	0.3900	2.88	0.1336
$C^2$	0.9807	0.3550	13.22	0.0083*
Residual				
Lack of fit	1.18	0.4220	3.34	0.1372

**Table 4.** Variance analysis of the regression models: dissecting the relationships between experimental factors (A, B, C) and response variables ( $Y_1$ ,  $Y_2$ ). Note: \*\* means extremely significant ( $P < 0.01$ ); \* means significant ( $P < 0.05$ ).

$$\begin{cases} Y_1 = 95.10 - 0.9387A + 0.43B - 1.01C + 2.16AB - 0.225AC \\ \quad - 0.0675BC - 0.4780A^2 - 0.3405B^2 - 0.3680C^2 \\ Y_2 = 37.94 - 7.23A + 5.29B - 1.08C - 5.34AB + 3.17AC \\ \quad + 0.885BC - 5.90A^2 - 3.16B^2 + 6.77C^2 \end{cases} \quad (26)$$

The  $P$ -values of the impurity removal rate ( $Y_1$ ) and film leakage rate ( $Y_2$ ) are all less than 0.01, indicating that the established regression models of  $Y_1$  and  $Y_2$  are highly significant. The  $P$ -values of the lack-of-fit terms are all greater than 0.05, indicating that the models have a high degree of fit. The coefficients of determination  $R^2$  of the models are 0.903 and 0.920, respectively, indicating that the models can explain more than 90% of the variability of the experimental data, and are suitable for the prediction of the impurity removal rate and film leakage rate of the separation device.

By analyzing the  $P$ -value of each factor, the effect of the factor on the impurity removal rate  $Y_1$  is in the order of feeding quantity C, fan rotational velocity A, disc rotational velocity B in descending order, and the effect on the film leakage rate  $Y_2$  is in the order of fan rotational velocity A, disc rotational velocity B, feeding quantity C in descending order.

#### Sensitivity analysis

To further analyze the response of the device's separation performance to parameter deviations, a parameter sensitivity analysis was conducted based on the Box-Behnken experiment. According to Table 3, the mean and range of the corresponding impurity removal rate and film leakage rate under different levels of each factor can be obtained. Under different levels of fan rotational velocity A, the mean values of the impurity removal rate are 95.20%, 94.78% and 93.33% respectively, with a range of 1.87%. The mean values of the film leakage rate are 41.08%, 39.54% and 26.62% respectively, with a range of 14.46%. Under different levels of disc rotational velocity B, the mean values of the impurity removal rate are 93.90%, 94.72% and 94.76% respectively, with a range of 0.86%. The mean values of the film leakage rate are 29.92%, 38.32% and 40.51% respectively, with a range of 10.59%. Under different levels of feeding quantity C, the mean values of the impurity removal rate are 95.33%, 94.73% and 93.31% respectively, with a range of 2.02%. The mean values of the film leakage rate are 41.25%, 33.91% and 39.10% respectively, with a range of 7.34%. Thus, C causes the largest range of the impurity removal rate, while B causes the smallest range. This indicates that the change of C has the greatest influence on the impurity removal rate, followed by A, and B has the least influence. A causes the largest range of the film leakage rate, while C causes the smallest range. This shows that A has the greatest influence on the film leakage rate, followed by B, and C has the least influence. This is consistent with the results of the factor significance analysis of variance given in Table 4.

The sensitivity coefficient  $\mu$  is introduced for parameter sensitivity analysis<sup>27</sup>. Equation (27) gives the calculation method for the coefficient.

$$\mu = \left| \frac{x}{\Delta x} \times \frac{f(x + \Delta x) - f(x)}{f(x)} \right| \quad (27)$$

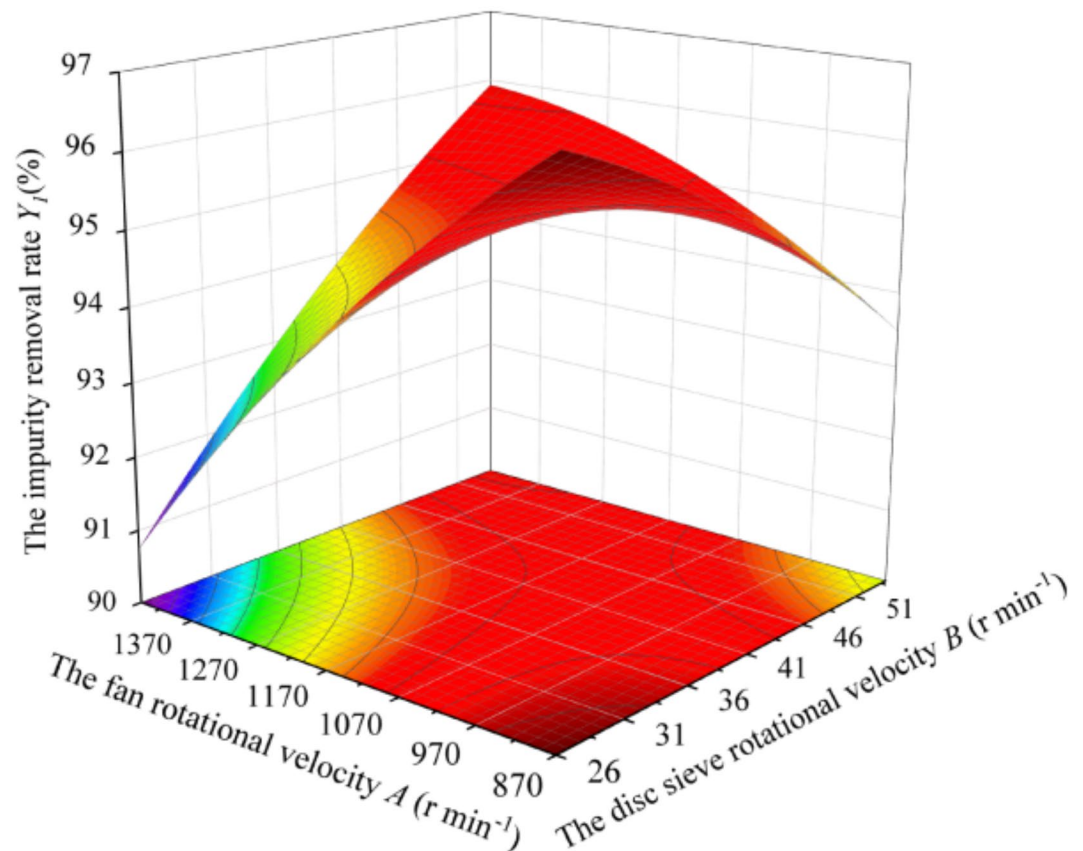
where,  $x$  is the initial input value of the parameter;  $\Delta x$  is the input variable value of the parameter;  $f(x)$  is the calculated output result corresponding to the initial input value;  $f(x + \Delta x)$  is the calculated output result corresponding to the variable value. The larger  $\mu$  is, the greater the influence of the parameter on the analysis index, and vice versa.

According to Eq. (27), the mean values of the sensitivity coefficients of the impurity removal rate under different levels of  $A$ ,  $B$  and  $C$  are 0.02, 0.01 and 0.02, respectively; the mean values of the sensitivity coefficients of the film leakage rate are 0.32, 0.43 and 0.26, respectively. Therefore, the sensitivity of  $A$ ,  $B$  and  $C$  to the impurity removal rate, from high to low, is  $A = C > B$ . However, the overall sensitivity levels of the three parameters to the impurity removal rate are relatively low. The sensitivity of  $A$ ,  $B$  and  $C$  to the film leakage rate, from high to low, is  $B > A > C$ . This is different from the above-mentioned analysis of variance and range analysis. The main reason is that the sensitivity coefficient analysis is based on the relative change ratio between parameters and results, which can effectively explain the relative influence degree. In contrast, the analysis of variance decomposes the total variation and comprehensively considers the influence of factors and their interactions on the results. The range analysis judges the importance of factors by comparing the ranges of test results under different levels of each factor, only considering the difference between the maximum and minimum values. Therefore, the results of the sensitivity coefficient analysis are also reasonable. As can be seen from the above analysis, the parameter changes have a relatively low sensitivity to the impurity removal rate and a relatively high sensitivity to the film leakage rate. That is, as the parameters change, the impurity removal rate varies within a small range, while the film leakage rate varies within a large range. Therefore, when considering the weight of the response targets of the impurity removal rate and the film leakage rate during the operation and optimization phases of the separation device, the priority and weight of the film leakage rate indicator can be moderately increased to ensure the stable and efficient operation of the device.

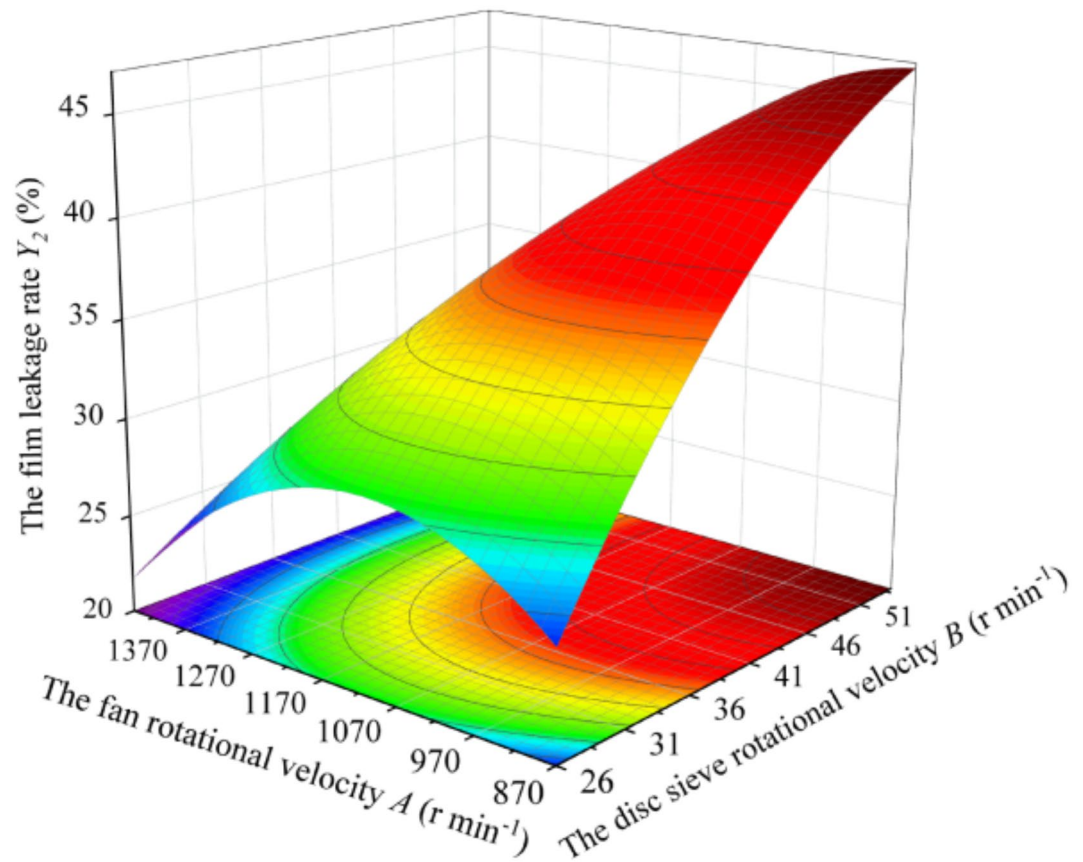
#### Response surface analysis

Figure 18 shows that the interaction of fan rotational velocity  $A$  and disc rotational velocity  $B$  influences the effect of the impurity removal rate  $Y_1$ , when the feeding quantity  $C$  is fixed at the central level ( $C = 154$  kg/h). When  $A$  is at a lower level,  $Y_1$  exhibits a decreasing trend with the increase of  $B$ . When  $A$  is at a higher level,  $Y_1$  shows a gradual increase with the increase of  $B$ . When  $B$  is at a lower level,  $Y_1$  exhibits a decreasing trend with the increase of  $A$ . When  $B$  is at a higher level,  $Y_1$  shows a gradually increasing trend with the increase of  $A$ .

Figure 19 shows that the interaction of the fan rotational velocity  $A$  and disc rotational velocity  $B$  affects the film leakage rate  $Y_2$ , when the feeding quantity  $C$  is fixed at the central level ( $C = 154$  kg/h). When  $A$  is at a lower level,  $Y_2$  shows an increasing tendency with the increase of  $B$ . When  $A$  is at a higher level,  $Y_2$  shows a tendency to increase firstly and then decrease with the increase of  $B$ . When  $B$  is at a lower level,  $Y_2$  tends to increase and then decrease with the increase of  $A$ . When  $B$  is at a higher level,  $Y_2$  tends to decrease with the increase of  $A$ .



**Fig. 18.** The surface plot of impurity removal rate response, generated by Origin 2018 software. It shows the interactive effects of fan rotational velocity  $A$  and disc rotational velocity  $B$  on impurity removal rate  $Y_1$ .



**Fig. 19.** The surface plot of film leakage rate response, generated by Origin 2018 software. It shows the interactive effects of fan rotational velocity  $A$  and disc rotational velocity  $B$  on the film leakage rate  $Y_2$ .

Reason analysis: When the disc rotational velocity  $B$  ( $B=26$  r/min) is at a lower level, the film and impurity materials maintain a low-velocity migration. The vertical displacement after the collision with the disc is small, and there is basically no gap between the material layers. According to Eq. (17), when the materials move along the sieve disc, the velocity difference between the residual films and the straw-soil mixture is small, the relative motion trend is weak, and separation is difficult. Owing to the coverage of the straw-soil mixture, the effect of airflow on residual films is weakened. The residual films pressed underneath are transported with the movement of the cotton straw and soil to the cotton and soil impurity collection boxes. Consequently, the impurity removal rate  $Y_1$  decreases, and the film leakage rate  $Y_2$  increases. As the fan rotational velocity  $A$  increases from 1120 to 1450 r/min, the wind force continues to strengthen. In this case, the surface layer of broken straw and soil particles with a small mass overcome gravity and are transported to the residual film collection box under the action of airflow. The force component of gravity of the straw-soil mixture in the normal direction is partially offset by the wind force, the pressure on the residual films is reduced, and the bonding strength between the residual film layers is reduced. The broken films (the maximum outside dimensions in the range of 0 ~ 100 mm) are drilled from the gap of the residual film layers, and migrated to the residual film collection box under the action of air flow. As a result, the impurity removal rate  $Y_1$  continues to decrease, and the film leakage rate  $Y_2$  gradually decreases.

When the disc rotational velocity  $B$  ( $B=54$  r/min) is at a higher level, the film and impurity materials maintain rapid transport. The vertical displacement after the collision is large, and the gaps are generated between the material layers. When moving along the sieve surface, the velocity difference between the residual films and the straw-soil mixture is large, the relative motion trend is obvious, and it is easy to separate. In the process of movement, the broken films drill out from the gap between the material layers, and move to the residual film collection box under the action of air flow. As the fan rotational velocity  $A$  increases from 870 to 1450 r/min, the wind force continues to increase, and the pressure of the straw-soil mixture on the residual films decreases. In this case, the acceleration and motion velocity of the residual films in the vertical direction gradually increase, and the films are rapidly transported to the residual film collection box. As a result, the impurity removal rate  $Y_1$  gradually decreases, and the film leakage rate  $Y_2$  gradually decreases.

When the fan rotational velocity  $A$  ( $A=870$  r/min) is at a lower level, the wind force is small. With the disc rotational velocity  $B$  increasing from 26 to 54 r/min, the transport velocity of the film and impurity materials increases. The velocity difference between the residual films and the straw-soil mixture also increases, and the separation tendency is enhanced. Due to the insufficient airflow intensity and the short time of full contact with the airflow, when the residual films are separated from the straw-soil mixture, there are fewer residual films that

Items	Impurity removal rate $Y_1$ (%)	Film leakage rate $Y_2$ (%)
Predicted value	96.51	21.92
Physical test values 1	91.32	27.43
Physical test values 2	93.44	26.69
Physical test values 3	90.93	27.55
Average value of physical tests	91.90	27.22

**Table 5.** Optimization results for maximizing  $Y_1$  and minimizing  $Y_2$ .

can be transported to the residual film collection box. After migrating through the suction hood, the residual films are mixed with the straw-soil mixture. As a result, the impurity removal rate  $Y_1$  gradually decreases, and the film leakage rate  $Y_2$  gradually increases.

When the fan rotational velocity  $A$  ( $A = 1450$  r/min) is at a higher level, the wind force is large. With the disc rotational velocity  $B$  increasing from 26 to 39 r/min, the transport velocity of the film and impurity materials gradually increases. The vertical displacement after the collision gradually increases, and the gaps between the material layers gradually become more. When moving along the sieve surface, the separation trend of the residual films from the straw-soil mixture increases, the pressure of the straw-soil mixture on the residual films gradually weakens, and the amount of residual film migrating to the residual film collection box increases. During the movement, the broken films drill out from the gap between the material layers, and maintain a slower migration velocity. In this case, the broken films leak directly from the sieve disc gap before reaching the double action area. As a result, both the impurity removal rate  $Y_1$  and the film leakage rate  $Y_2$  gradually increase. With the disc rotational velocity  $B$  increasing from 39 to 54 r/min, the separation trend of the residual films from the straw-soil mixture continues to increase, and the amount of residual film migrating to the residual film collection box continues to increase. During the movement process, the broken films drill out from the gap, and maintain a faster migration velocity. In this case, the broken films quickly move to the double action area, and are transported to the residual film collection box under the action of the airflow. As a result, the impurity removal rate increases, while the film leakage rate decreases.

#### Parameter optimization

The impurity removal rate is related to the purity and quality of the separated residual films, while the film leakage rate is related to processing costs, production continuity and environmental impact. From the perspective of actual production, the main purpose of designing this separation device is to provide key pretreatment technical equipment for the resource utilization of waste residual films. By doing so, it can reduce the environmental pollution caused by plastic films and improve the efficiency of resource utilization. When this separation device is used to process the film-impurity mixture, it can yield relatively clean residual films. This, in turn, raises the added value of the residual films and boosts economic benefits. Therefore, it is necessary to ensure the highest impurity removal rate first, and secondly, to keep the film leakage rate at a relatively low level, to improve the resource utilization rate of residual films. Taking the maximum impurity removal rate  $Y_1$  and the minimum film leakage rate  $Y_2$  as the optimization objectives, the optimization module in the Design-Expert 13 data analysis software is used to optimize the target. The objective function and constraint conditions are as listed in Eq. (28) below.

$$\begin{cases} \max Y_1(A, B, C) \\ \min Y_2(A, B, C) \\ 870r/\min \leq A \leq 1450r/\min \\ 26r/\min \leq B \leq 54r/\min \\ 110kg/h \leq C \leq 198kg/h \end{cases} \quad (28)$$

The optimal parameter combination for the device is obtained as follows: fan rotational velocity is 1450 r/min, disc rotational velocity is 54 r/min, and feeding quantity is 130 kg/h. The theoretical values of the separation performance index after optimization are: the impurity removal rate  $Y_1$  is 96.51%, and the film leakage rate  $Y_2$  is 21.92%. Table 5 depicts the optimization results for maximizing impurity removal rate  $Y_1$  and minimizing film leakage rate  $Y_2$ .

As shown in Table 5, a physical verification test was carried out, and the results show that the average impurity removal rate is 91.90%, the average film leakage rate is 27.22%, and the error between the physical test value and the predicted value is 4.61% and 5.30%, respectively. The reasons for the errors may be the non-uniformity of the film-impurity materials. For example, the caking and uneven distribution of residual films and impurities may lead to insufficient representativeness of each sample taken. Another possible cause is the human-related factors in the test operation process. For instance, the uniformity of film-impurity material feeding and the timing of equipment start-up and shutdown can interfere with the test results. Although there are errors between the predicted values and the actual test results, the errors are small. It still indicates that the parameter optimization has relatively high reliability, and the constructed response model has good predictability. Subsequently, regarding the sample selection issue, more scientific sampling methods, such as multi-point sampling and stratified sampling followed by uniform mixing before measurement, will be adopted to ensure the representativeness of the samples. For the test operation issue, detailed operation specifications

and procedures will be formulated, and the operators will be trained to reduce errors caused by human factors. Meanwhile, in the process of test data processing, reasonable statistical methods and error analysis models, such as taking the average of multiple measurements and conducting uncertainty analysis, will be used to improve the accuracy and reliability of the test results.

## Conclusions

- (1) Before contacting the sieve disc, the motion state of the film and impurity materials in the windless area is affected by the factors such as the initial velocity and throwing angle; the motion state in the windy area is affected by the factors such as the mass, airflow velocity and windward area. In the collision stage, the motion state is affected by the factors such as the mass, airflow velocity, contact area with the sieve discs and compression amount of the material. In the relative motion stage, the motion state is affected by the factors such as the mass, disc rotational velocity, sieve disc structure size, airflow velocity, windward area, friction coefficients and residual film material layer thickness. Through analysis, it is determined that the main factors affecting the motion state are the feeding quantity, airflow velocity (fan rotational velocity) and disc rotational velocity.
- (2) A Box-Behnken response surface experiment was carried out, and the regression models of feeding quantity, fan rotational velocity and disc rotational velocity on the impurity removal rate and the film leakage rate are established, respectively. Through the analysis of variance, it is determined that the order of influence on the impurity removal rate from large to small is: feeding quantity, fan rotational velocity, disc rotational velocity; the order of influence on the film leakage rate from large to small is: fan rotational velocity, disc rotational velocity, feeding quantity. Through the dual-objective optimization solution, the optimal parameter combination of the device is obtained: the fan rotational velocity is 1450 r/min, the disc rotational velocity is 54 r/min, and the feeding quantity is 130 kg/h. The corresponding impurity removal rate is 96.51%, and the film leakage rate is 21.92%. The average impurity removal rate of the verification test is 91.90%, the average film leakage rate is 27.22%, and the errors between the predicted value and the physical test values are 4.61% and 5.30%, respectively. This indicates that the established regression models are reliable and have a certain reference value.

## Discussion

Currently, the separation of the film-impurity mixture mainly relies on manual sorting, which has problems such as high labor intensity, low production efficiency, high production costs and poor working conditions. After the separation of residual films, the main utilization method is recycling granulation, which converts the recovered films into relatively low-end products, such as drip irrigation tapes or turnover baskets. Compared with the traditional manual sorting method, this device shows certain advantages. In terms of energy consumption, it has a high energy utilization rate when processing materials per unit area, resulting in lower energy-consumption costs. In the aspect of impurity disposal, the normal operation of the device reduces labor costs. Moreover, the separated impurities can be further classified for recycling or properly disposed of, avoiding secondary pollution, which is in line with the concept of sustainable development. Regarding environmental impact, the device can operate continuously, greatly improving the resource utilization efficiency of residual films, reducing the environmental pollution caused by the plastics, and promoting the green and sustainable development of agricultural production. Meanwhile, the physical effects such as mechanical vibration and airflow noise generated during its operation are at a relatively low level, resulting in less dust rising. This reduces the health risks for operators exposed to a high-dust environment for a long time.

However, the device still has some potential limitations. In terms of operating performance, the film-impurity separation device designed in this study has an impurity removal rate of over 90%, but the film leakage rate exceeds 20%. This indicates that the device performs well in promoting the separation of residual films from impurities, yet the utilization rate of raw materials is slightly insufficient. The possible reasons for this are as follows. First, the moisture content of the film-impurity mixture, closely related to the harvest weather, is relatively high, making the films extremely likely to adhere to each other. For instance, when harvesting in the early morning with heavy dew, the moisture content of the materials will increase significantly. Moreover, the currently recycled film-impurity mixtures are transported in bales, and this method makes it difficult for the moisture inside the mixture to evaporate. Second, when the film-impurity bales are pre-processed by crushing, the uniformity of their crushing scale and spatial distribution is poor, which in turn interferes with the separation performance of the device. Finally, as for the design of the device structure, there is still a need for further optimization to reduce the film leakage rate.

In the future, regarding the environmental factors, especially the impact of humidity, a pre-treatment process will be added at the front end of the feeding section, and drying equipment will be used to remove the moisture from the materials. To address the issues of non-uniform particle size and distribution of the operating objects, from the perspective of the material composition of residual films and impurities, a simulation model of the film-impurity mixture will be established to control the consistency of the materials, which is convenient for the study of the device mechanism. Based on this, the gas-solid coupling method will be used to study the movement and dynamic characteristics of the device, as well as the influence of structural and operating parameters on the movement state of the materials. For the optimization of the device structure, measures such as adjusting the airflow velocity distribution, optimizing the structural parameters of the disc sieve, or adding a secondary separation stage will be taken to reduce the film leakage rate while ensuring a high impurity removal rate. For the mixture of residual films and impurities under the sieve, in-depth resource utilization will be carried out by developing process routes for manufacturing artificial stalk-plastic boards and autoclaved aerated blocks using this mixture as raw materials.

## Data availability

The data that support the findings of this study are available on request from the corresponding author Z.K., under reasonable request.

Received: 6 December 2024; Accepted: 3 March 2025

Published online: 05 March 2025

## References

- Wang, H. B. et al. Alternative planting patterns of film-mulching cotton for alleviating plastic residue pollution in Aksu Oasis, Southern Xinjiang. *Ind. Crops Prod.* **203**, 117205. <https://doi.org/10.1016/j.indcrop.2023.117205> (2023).
- Zhou, X. C. et al. Design and test of film lifting separation conveying device of stripper-plate-type residual film recovery machine. *J. Shihezi Univ. (Nat. Sci.)* **04**, 472–480. <https://doi.org/10.13880/j.cnki.65-1174/n.2022.21.021> (2022).
- Gou, H. X., Wen, H. J. & Chen, X. G. Design and test of the two-order pin-tooth chain plate type residual film recovery device. *Trans. Chin. Soc. Agric. Eng. (Trans. CSAE)* **40**(19), 1–11. <https://doi.org/10.11975/j.issn.1002-6819.202403041> (2024).
- Jiang, D. L., Yan, L. M., Chen, X. G., Mo, Y. S. & Yang, J. C. Design and experiment of nail tooth picking up device for strip type residual film recycling and baling machine. *Int. J. Agric. Biol. Eng.* **16**(6), 85–96. <https://doi.org/10.25165/j.ijabe.20231606.7563> (2023).
- Xie, J. H. et al. Design and test of crushing and kneading device for machine harvested cotton field residual film mixture. *Trans. Chin. Soc. Agric. Mach.* **55**(3), 133–143. <https://doi.org/10.6041/j.issn.1000-1298.2024.03.013> (2024).
- Zhang, J. F. et al. Current situation and countermeasures of residual plastic film pollution in farmland. *Soils Crops* **11**(4), 385–397. <https://doi.org/10.11689/j.issn.2095-2961.2022.04.003> (2022).
- Li, W. T., Yang, S. W. & Han, X. Y. Research progress on control methods of agricultural plastic film pollution in China. *J. Anhui Agric. Sci.* **50**(16), 10–131. <https://doi.org/10.3969/j.issn.0517-6611.2022.16.003> (2022).
- Dong, H. L., Zhang, K. P., Zhang, P., Yang, Y. & Sun, B. G. Research status and prospect of rapeseed harvesting technology in cold and drought region. *J. Chin. Agric. Mech.* **39**(12), 25–29. <https://doi.org/10.13733/j.jcam.issn.2095-5553.2018.12.04> (2018).
- Niu, C. H., Shi, X., Jiang, Y. X., Yang, H. M. & Qiao, Y. Y. Design and test on type of waste plastic mulch films and Impurities winnowing machine. *Xinjiang Agric. Mech.* **05**, 23–25. <https://doi.org/10.13620/j.cnki.issn1007-7782.2018.05.007> (2018).
- Kang, J. M. et al. Aerodynamic characteristics of residual film materials and test of membrane separation device. *J. Chin. Agric. Mech.* **41**(01), 167–172. <https://doi.org/10.13733/j.jcam.issn.2095-5553.2020.01.30> (2020).
- Peng, Q. J., Li, C. S., Kang, J. M., Shi, G. K. & Zhang, H. Improved design and test on pneumatic cylinder sieve film hybrid separator. *Trans. Chin. Soc. Agric. Mach.* **51**(8), 126–135. <https://doi.org/10.6041/j.issn.1000-1298.2020.08.014> (2020).
- Zhang, B. C. et al. Enhancing resource utilization: A novel method for effective separation of residual film and impurities in cotton fields. *J. Environ. Manag.* **359**, 121065. <https://doi.org/10.1016/j.jenvman.2024.121065> (2024).
- Kang, J. M. et al. Design and test of screen hole clearing device for Trommel sieve type membrane miscellaneous wind separator. *Trans. Chin. Soc. Agric. Mach.* **53**(09), 91–98. <https://doi.org/10.6041/j.issn.1000-1298.2022.09.009> (2022).
- Xie, C. S. et al. Optimization of screen-hole-clearing devices for mechanized residual film-impurity separation. *Appl. Sci. Basel* **12**(22), 11658. <https://doi.org/10.3390/app122211658> (2022).
- Fu, J. et al. Machine-vision-based algorithm for blockage recognition of Jittering sieve in corn harvester. *Appl. Sci.* **10**(18), 6319. <https://doi.org/10.3390/app10186319> (2020).
- Ma, Z. et al. BP neural network model for material distribution prediction based on variable amplitude anti-blocking screening DEM simulations. *Int. J. Agric. Biol. Eng.* **16**(4), 190–199. <https://doi.org/10.25165/j.ijabe.20231604.7178> (2023).
- Ashkiki, A. R., Felske, C. & McCartney, D. Impacts of seasonal variation and operating parameters on double-stage Trommel performance. *Waste Manag.* (86), 36–48. <https://doi.org/10.1016/j.wasman.2019.01.026> (2019).
- Zhang, Y., Xu, B. G. & Wang, X. Z. Study and design of disk screens for municipal solid waste separation. *CFHI Technol.* (06), 26–29. <https://doi.org/10.3969/j.issn.1673-3355.2015.06.007> (2015).
- Peng, X. B. Design and experiment of alternated multi-sieve device with function of separating soil from residual film mixture. Master's Thesis, Shihezi University, Shihezi, China. (2021). <https://d.wanfangdata.com.cn/thesis/D02505211>
- Zhou, P. F. et al. Design and experiment of Trommel with function of separating soil from residual film mixture. *J. Jilin Univ. (Eng. Technol. Ed.)* (09), 2718–2731. <https://doi.org/10.13229/j.cnki.jdxbgxb.20211267> (2023).
- Song, J. et al. Analysis of impact and absorbed energy of *Fritillaria ussuriensis* Maxim during drum screening and its effect on impact damage. *Comput. Electron. Agric.* **215**. <https://doi.org/10.1016/j.compag.2023.108368> (2023).
- Fang, M., Yu, Z. H. & Zhang, W. J. Dynamic analysis of material motion using MATLAB / Simulation environment and test verification. *Adv. Mech. Eng.* **12**(9), 1–14. <https://doi.org/10.1177/1687814020957806> (2020).
- Fang, M. et al. Analysis and experiments of the movement process for the shredded material of disc knife chaff cutter. *Trans. Chin. Soc. Agric. Eng.* **37**(7), 76–84. <https://doi.org/10.11975/j.issn.1002-6819.2021.07.010> (2021).
- Wang, X. S., Liu, D. W., Xie, F. P., Li, X. & Wu, B. Motion analysis of ejected grain in cyclone cleaning separation cylinder. *Times Agric. Mach.* **46**(03), 104–108. <https://doi.org/10.3969/j.issn.1007-8320.2019.03.048> (2019).
- Zhang, X. & Li, L. Reflection and transmission of elastic waves at the interface between elastic and viscoelastic solids. *J. Sci. Teachers' Coll. Univ.* **44**(12), 44–49. <https://doi.org/10.3969/j.issn.1007-9831.2024.12.007> (2024).
- Li, Y. B. et al. Improving particle dispersion characteristics with a novel cleaning screen: Parameter design and numerical simulation. *Powder Technol.* **397**, 116987. <https://doi.org/10.1016/j.powtec.2021.11.031> (2022).
- Meng, C. et al. Sensitivity analysis and inversion of HSS model parameters for soft soil layers on the first terrace of the Yangtze river. *Acta Scientiarum Naturalium Universitatis Sunyatseni* 1–9. <https://doi.org/10.13471/j.cnki.acta.snus.ZR20240264> (2024).

## Author contributions

Conceptualization, J.L., X.W., H.M. and Z.K.; methodology, J.L., F.D. and Y.F.; software, J.L. and Y.F.; validation, J.L. and F.D.; data curation, J.L. and Y.F.; writing—original draft preparation, J.L.; writing—review and editing, J.L., H.P., X.W., H.M. and Z.K.; project administration, F.D.; funding acquisition, H.M. and Z.K. All authors have read and agreed to the published version of the manuscript.

## Funding

This work was supported by the National Natural Science Foundation of China [grant numbers 52360022], the national key research and development plan sub-project [grant numbers 2023YFD170190403] and Jiangsu Province and Education Ministry Co-Sponsored Synergistic Innovation Center of Modern Agricultural Equipment [Grant Numbers XTCX2006].

## Declarations

### Competing interests

The authors declare no competing interests.

### Additional information

**Correspondence** and requests for materials should be addressed to H.M. or Z.K.

**Reprints and permissions information** is available at [www.nature.com/reprints](http://www.nature.com/reprints).

**Publisher's note** Springer Nature remains neutral with regard to jurisdictional claims in published maps and institutional affiliations.

**Open Access** This article is licensed under a Creative Commons Attribution-NonCommercial-NoDerivatives 4.0 International License, which permits any non-commercial use, sharing, distribution and reproduction in any medium or format, as long as you give appropriate credit to the original author(s) and the source, provide a link to the Creative Commons licence, and indicate if you modified the licensed material. You do not have permission under this licence to share adapted material derived from this article or parts of it. The images or other third party material in this article are included in the article's Creative Commons licence, unless indicated otherwise in a credit line to the material. If material is not included in the article's Creative Commons licence and your intended use is not permitted by statutory regulation or exceeds the permitted use, you will need to obtain permission directly from the copyright holder. To view a copy of this licence, visit <http://creativecommons.org/licenses/by-nc-nd/4.0/>.

© The Author(s) 2025